Mon. Not. R. Astron. Soc. **000**, 000–000 (0000) Printed 15 July 2016 (MN LATEX style file v2.2)

# Predicting polarization signatures for double-detonation and delayed-detonation models of Type Ia supernovae

M. Bulla,[1⋆] S. A. Sim,[1,2] M. Kromer,[3] I. R. Seitenzahl,[2,4] M. Fink,[5] F. Ciaraldi-Schoolmann,[6] F. K. Röpke,[7,8] W. Hillebrandt,[6] R. Pakmor,[7] A. J. Ruiter[2,4] and S. Taubenberger[6,9]

[1] *Astrophysics Research Centre, School of Mathematics and Physics, Queen's University Belfast, Belfast BT7 1NN, UK*
[2] *ARC Centre of Excellence for All-sky Astrophysics (CAASTRO)*
[3] *The Oskar Klein Centre and Department of Astronomy, Stockholm University, AlbaNova, SE-106 91 Stockholm, Sweden*
[4] *Research School of Astronomy and Astrophysics, Australian National University, Canberra, ACT 2611, Australia*
[5] *Institut für Theoretische Physik und Astrophysik, Universität Würzburg, Emil-Fischer-Straße 31, D-97074 Würzburg, Germany*
[6] *Max-Planck-Institut für Astrophysik, Karl-Schwarzschild-Str. 1, D-85748 Garching bei München, Germany*
[7] *Heidelberger Institut für Theoretische Studien, Schloss-Wolfsbrunnenweg 35, D-69118 Heidelberg, Germany*
[8] *Zentrum für Astronomie der Universität Heidelberg, Institut für Theoretische Astrophysik, Philosophenweg 12, D-69120 Heidelberg, Germany*
[9] *European Southern Observatory, Karl-Schwarzschild-Str. 2, D-85748 Garching, Germany*

arXiv:1607.04081v1 [astro-ph.HE] 14 Jul 2016

Accepted 2016 July 14. Received 2016 July 14; in original form 2016 April 21

**ABSTRACT**

Calculations of synthetic spectropolarimetry are one means to test multi-dimensional explosion models for Type Ia supernovae. In a recent paper, we demonstrated that the violent merger of a 1.1 and 0.9 $M_\odot$ white dwarf binary system is too asymmetric to explain the low polarization levels commonly observed in normal Type Ia supernovae. Here, we present polarization simulations for two alternative scenarios: the sub-Chandrasekhar mass double-detonation and the Chandrasekhar mass delayed-detonation model. Specifically, we study a two-dimensional double-detonation model and a three-dimensional delayed-detonation model, and calculate polarization spectra for multiple observer orientations in both cases. We find modest polarization levels ($< 1$ per cent) for both explosion models. Polarization in the continuum peaks at $\sim 0.1-0.3$ per cent and decreases after maximum light, in excellent agreement with spectropolarimetric data of normal Type Ia supernovae. Higher degrees of polarization are found across individual spectral lines. In particular, the synthetic Si II $\lambda$6355 profiles are polarized at levels that match remarkably well the values observed in normal Type Ia supernovae, while the low degrees of polarization predicted across the O I $\lambda$7774 region are consistent with the non-detection of this feature in current data. We conclude that our models can reproduce many of the characteristics of both flux and polarization spectra for well-studied Type Ia supernovae, such as SN 2001el and SN 2012fr. However, the two models considered here cannot account for the unusually high level of polarization observed in extreme cases such as SN 2004dt.

**Key words:** hydrodynamics – polarization – radiative transfer – methods: numerical – supernovae: general

## 1 INTRODUCTION

Despite their relevance to cosmology (Riess et al. 1998; Perlmutter et al. 1999), Type Ia supernovae (SNe Ia) are still poorly understood. While believed to stem from thermonuclear explosions of carbon-oxygen white dwarfs (WDs), answers to the questions of when, why and how these events are triggered remain unclear (Hillebrandt et al. 2013; Maoz et al. 2014). Recent explosion simulations have led to a better understanding of the physics involved, and comparisons of synthetic light curves and spectra with observations have played a key role in identifying which explosions scenarios are most promising. However, unambiguous discrimination between models is still challenging, even for the best observed nearby supernovae (Röpke et al. 2012).

Polarization offers a unique opportunity to discriminate

⋆ E-mail: mbulla01@qub.ac.uk

© 0000 RAS

between the variety of possible explosion scenarios. The observational evidence that SNe Ia are associated with rather low levels of polarization ($\lesssim 1$ per cent) demands modest asphericities in the progenitor system and/or explosion mechanism, thus providing the means to effectively test different explosion models. Although predictions have been made using idealized geometries with simple departures from spherical symmetry – such as ellipsoidal structures (Wang et al. 1997; Howell et al. 2001; Höflich et al. 2006; Patat et al. 2012), clumped and toroidal shells (Kasen et al. 2003) or large scale asymmetries associated with ejecta overrunning the companion star (Kasen et al. 2004) – until recently, no spectropolarimetric studies had been made for full multi-dimensional hydrodynamic explosion simulations. We have therefore started our long-term project aiming to predict polarization signatures for a series of modern SN Ia hydrodynamic models. In the first paper of this series (Bulla et al. 2016), we have demonstrated the power of this approach for the violent merger of two 1.1 and 0.9 $M_\odot$ WDs as presented by Pakmor et al. (2012). Despite matching luminosities and spectra of normal SNe Ia reasonably well, this model was found to be too asymmetric to reproduce the polarization levels seen for the majority of normal SNe Ia.

In this second paper, we carry out polarization spectral synthesis for examples of two alternative scenarios: the "delayed-detonation" of a near Chandrasekhar mass ($M_{ch}$) WD and the "double-detonation" of a sub-$M_{ch}$ WD. In the "delayed-detonation" model (e.g. Khokhlov 1991; Höflich et al. 1995; Plewa et al. 2004; Röpke & Niemeyer 2007; Kasen et al. 2009; Blondin et al. 2013; Seitenzahl et al. 2013), a WD is thought to accrete material from a non-degenerate companion star and explode following carbon ignition near the WD centre which occurs when the mass has grown close to $M_{ch}$. Initially, a carbon deflagration is ignited but delayed-detonation models posit that during the evolution of the explosion a detonation occurs. The second scenario we consider, the "double-detonation" model (e.g. Nomoto 1980; Taam 1980; Livne 1990; Shen & Bildsten 2009; Fink et al. 2010; Moll & Woosley 2013), describes the explosion of a sub-$M_{ch}$ WD. In this model, the explosion is triggered by the detonation of a helium surface layer that has been accreted from a helium-rich companion star. The shock wave from this detonation then triggers a second detonation in the core. Both delayed-detonation and double-detonation scenarios have received considerable attention over the past decade as they reproduce SN Ia light curves and spectra reasonably well (Höflich et al. 1995; Höflich & Khokhlov 1996; Kasen et al. 2009; Kromer et al. 2010; Röpke et al. 2012; Sim et al. 2013; Blondin et al. 2015) and could provide an important contribution to the SN Ia population (e.g. Hachisu et al. 2008; Mennekens et al. 2010; Ruiter et al. 2011).

In this paper we perform polarization calculations for one explosion model of Fink et al. (2010) and one model of Seitenzahl et al. (2013). The former is chosen as it has been used in several studies (Scalzo et al. 2014a; Scalzo et al. 2014b; Childress et al. 2015; Kosenko et al. 2015) as a benchmark for the double-detonation scenario. The latter is selected since it has been widely used (Röpke et al. 2012; Summa et al. 2013; Scalzo et al. 2014a; Childress et al. 2015; Fransson & Jerkstrand 2015; Kosenko et al. 2015; Sneden et al. 2016) as representative of a class of delayed-detonation models in which a deflagration-to-detonation transition (DDT) is assumed to occur spontaneously during the propagation of the deflagration.

In Section 2 we summarize properties of the two specific explosion models, while in Section 3 we discuss the details of our radiative transfer calculations. We present synthetic observables for both models in Section 4 and comparisons with spectropolarimetric data of SNe Ia in Section 5. Finally, we discuss our results and draw conclusions in Section 6.

## 2 EXPLOSION MODELS

In this section we give a brief description of the two explosion models investigated in this study: a double-detonation model (selected from the study by Fink et al. 2010) and a delayed-detonation model (from Seitenzahl et al. 2013). We note that neither of the models we consider is perfect: in both cases, previous studies (see below) have identified shortcomings in matching observed spectra and light curve properties of normal SNe Ia. Nevertheless, we adopt these two example models as the most promising from the Fink et al. and Seitenzahl et al. series, respectively, and will focus on the added value of synthetic spectropolarimetry in understanding the strengths and weaknesses of their respective explosion scenarios.

### 2.1 Sub-$M_{ch}$ double-detonation model

The six double-detonation models investigated by Fink et al. (2010) comprise WDs with carbon-oxygen core masses increasing from 0.81 to 1.38 $M_\odot$ and helium-shell masses decreasing from 0.13 to $3.5\times10^{-3}$ $M_\odot$. The specific helium-shell masses were selected to meet minimum conditions required for a helium detonation suggested by Bildsten et al. (2007). Hydrodynamic simulations were performed in two-dimensions (2D) adopting azimuthal symmetry about the $z$ axis. In all the models, the first detonation is ignited at a single point on the positive $z$ axis at the interface between the core and the helium shell. While the detonation wave sweeps along the core-shell interface, a shock wave moves through the core and converges at an off-centre point on the negative $z$ axis (Livne & Glasner 1990). A second detonation is then initiated around this point if temperature and pressure conditions are sufficiently high (Niemeyer & Woosley 1997; Röpke et al. 2007). We note that, although this model is only 2D, neither the adopted WD progenitor model nor the ignition condition break axi-symmetry and thus it is expected to be a good approximation that azimuthal symmetry is preserved.

For our spectropolarimetric study, we select 'model 3' of Fink et al. (2010) since this configuration produces an amount of $^{56}$Ni (0.55 $M_\odot$) in the range observed for normal SNe Ia (Stritzinger et al. 2006; Scalzo et al. 2014a; Childress et al. 2015) and is found to predict observables in reasonable – although not perfect – agreement with normal SNe Ia (Kromer et al. 2010). This model (referred to as the D-DET model in the rest of the paper) has a carbon-oxygen core of 1.025 $M_\odot$ and a helium shell of 0.055 $M_\odot$. Owing to the low densities in the *shell*, 60 per cent of the helium is left unburned and much of the material that is burned does not reach nuclear statistical-equilibrium (NSE). Specifically, the conditions in the model favour burning products

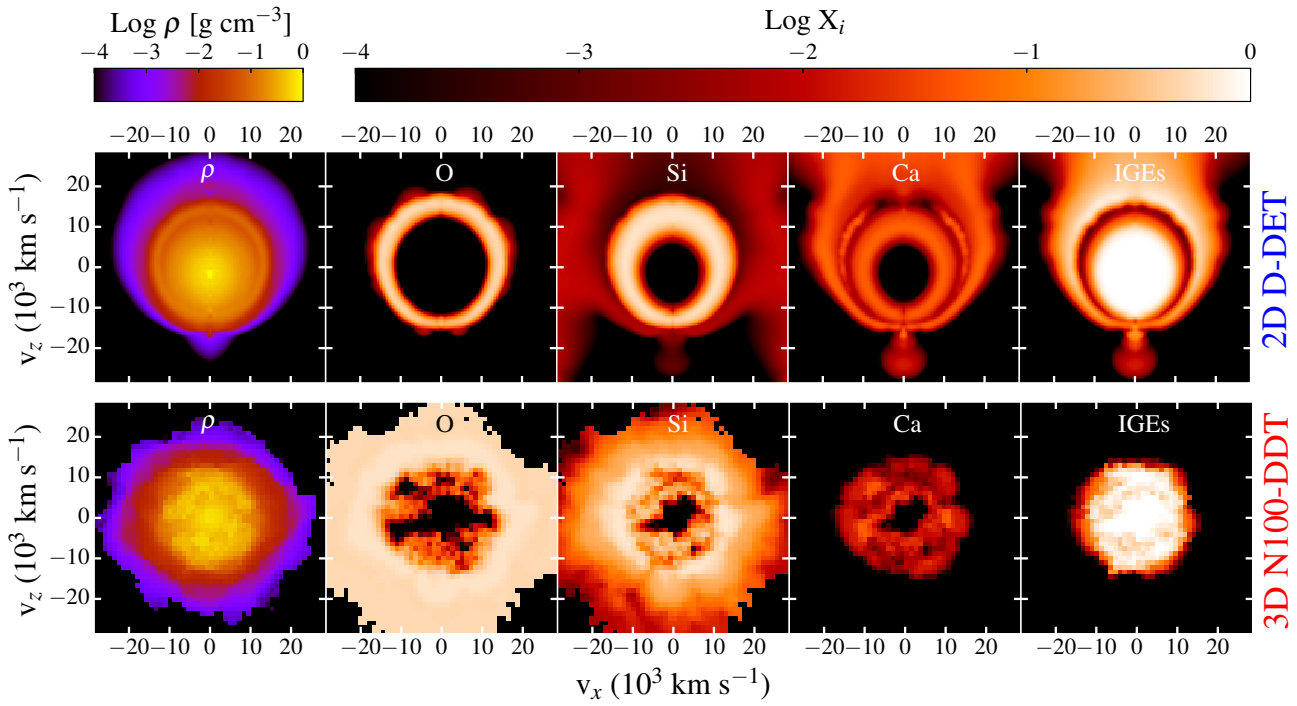


**Figure 1.** Density and composition of the ejecta 100 s after explosion for the 2D D-DET (upper panels) and 3D N100-DDT (bottom panels) models studied in this work. The density $\rho$ and mass fractions $X_i$ of oxygen, silicon, calcium and IGEs (summed from scandium to zinc) are shown in the $x$-$z$ plane.

rich in iron-group-elements (IGEs) lighter than $^{56}$Ni, such as $^{52}$Fe (11 per cent), $^{48}$Cr (8 per cent) and $^{44}$Ti (6 per cent). Aside from modest fractions of $^{40}$Ca (4 per cent) and $^{36}$Ar (4 per cent), very few intermediate-mass elements (IMEs) are produced in the shell. In contrast, the *core* detonation synthesizes 0.55 $M_\odot$ of $^{56}$Ni (96 per cent of the total IGE production in the core) and 0.37 $M_\odot$ of IMEs.

The upper panels in Fig. 1 show the density and composition of the ejecta when the system has already entered the homologous expansion phase ($\sim$ 8 s after explosion). Due to the asymmetries introduced by the explosion mechanism, the ejecta structure is fairly aspherical[1]. First, since the helium detonation is ignited in a point on the positive $z$-axis, ejecta from the *shell* (e.g. the outer layer of calcium) are distributed over a wider range of velocities in the northern compared to the southern hemisphere. Second, the off-center ignition of the *core* detonation causes the northern regions of the core to be less compressed than those on the opposite side. This has the effect of producing IMEs (e.g. silicon) that are more abundant and extend over a wider velocity range in the northern compared to the southern hemisphere (see also section 4.3 of Fink et al. 2010).

[1] We note that the specific ejecta morphology depends on the ignition geometry. Asymmetries produced in the D-DET model of Fink et al. (2010) follow from the choice of a one-point ignition on the $z$-axis, while more symmetric ejecta are expected for more symmetric shell ignitions (see Fink et al. 2007).

### 2.2 $M_{ch}$ DDT model

The set of three-dimensional (3D) DDT models studied by Seitenzahl et al. (2013) comprises WDs with mass close to $M_{ch}$. Twelve of the fourteen models differ only in ignition geometry of the deflagration (parametrized in terms of a number of spherical ignition kernels, ranging from 1 to 1600). The remaining two models are alternative versions of the 100-kernel model that consider different WD central densities. For all the models, the kernels were placed near the centre of the WD. Following the ignition, the deflagration flame propagates and turbulence develops. Once the turbulent velocity fluctuations at the flame front become sufficiently strong (Ciaraldi-Schoolmann et al. 2013; Seitenzahl et al. 2013), a transition to a supersonic detonation is invoked, which totally disrupts the WD.

For our spectropolarimetric study, we select the 'N100' model of Seitenzahl et al. (2013). This model (hereafter referred to as N100-DDT model) is chosen as it yields an amount of $^{56}$Ni ($0.6 M_\odot$) consistent with the values derived for the bulk of normal SNe Ia (Stritzinger et al. 2006; Scalzo et al. 2014a; Childress et al. 2015) and because it provides a good match to observed spectra and light curves (Röpke et al. 2012; Sim et al. 2013). This specific configuration produces 0.84 $M_\odot$ of IGEs and 0.45 $M_\odot$ of IMEs.

The lower panels of Fig. 1 show the density and composition of the ejecta for this model 100 s after explosion. The rather symmetric ignition geometry of this specific explosion simulation results in an overall spherical distribution of the yields. However, there are clear small-scale asymmetries in the oxygen and IME distributions that can be expected to imprint observable signatures.

## 3 SIMULATIONS

### 3.1 Radiative transfer calculations

To extract synthetic observables for the explosion models presented in Section 2, we carried out calculations using our 3D Monte Carlo (MC) radiative transfer code ARTIS (Sim 2007; Kromer & Sim 2009; Bulla et al. 2015). Radiative transfer calculations for the same D-DET and N100-DDT models were already performed by Kromer et al. (2010) and Sim et al. (2013), respectively, but here we present new simulations that include polarization. We first remap each explosion model to a Cartesian grid: in line with the previous studies, we remap the 2D D-DET model to a $100^3$ grid and the 3D N100-DDT model to a $50^3$ grid. We then follow the propagation of $N_{\rm q}$ MC quanta from 2 to 120 d after explosion using a series of 111 logarithmically spaced time-steps. We assume local thermodynamic equilibrium for the first 10 time-steps ($t < 2.95$ d) and a grey approximation for optically thick cells (Kromer & Sim 2009). Compared to Kromer et al. (2010) and Sim et al. (2013), here we use a more extended atomic data set (Gall et al. 2012) that includes about $8.6 \times 10^6$ lines and ions I - VII for $20 < {\rm Z} < 29$. Moreover, in order to achieve low MC noise levels in the polarization spectra (see also Section 3.2), we utilize a larger number of MC quanta, $N_{\rm q} = 5.12 \times 10^8$, for both the D-DET (cf. with $N_{\rm q} = 2 \times 10^7$ of Kromer et al. 2010) and the N100-DDT (cf. with $N_{\rm q} = 1.024 \times 10^8$ of Sim et al. 2013) model.

Following the technique described by Bulla et al. (2015), we extract high signal-to-noise synthetic observables for specific observer orientations. For the 2D D-DET model, we select three orientations in the $x$-$z$ plane[2] so that the ejecta asymmetries are properly sampled from north to south pole (see left panels of Fig. 2): $\boldsymbol{l_1} = (1/\sqrt{2}, 0, 1/\sqrt{2})$, $\boldsymbol{l_2} = (1, 0, 0)$, $\boldsymbol{l_3} = (1/\sqrt{2}, 0, -1/\sqrt{2})$. For the 3D N100-DDT model, we select five observer orientations (see right panels of Fig. 3). Guided by the findings of Sim et al. (2013), we first choose the orientations for which the model is brightest, $\boldsymbol{n_1} = (0, 0, -1)$, and faintest, $\boldsymbol{n_2} = (-1/\sqrt{2}, 1/\sqrt{2}, 0)$, and then select three additional directions to sample the plane defined by $\boldsymbol{n_1}$ and $\boldsymbol{n_2}$: $\boldsymbol{n_3} = (-1/2, 1/2, 1/\sqrt{2})$, $\boldsymbol{n_4} = (0, 0, 1)$ and $\boldsymbol{n_5} = (1/\sqrt{2}, -1/\sqrt{2}, 0)$. Flux and polarization spectra are extracted for each orientation between 10 and 30 d after explosion in the wavelength range 3500−10 000 Å. To decrease the MC noise levels in the red regions of the polarization spectra – where the flux is lower – we perform additional simulations with $N_{\rm q} = 2 \times 10^8$ and restricting to wavelengths larger than 5800 Å (see Bulla et al. 2015).

To map out the range of polarization covered by the explosion models, we also carried out two calculations with fewer packets ($N_{\rm q} = 1.5 \times 10^8$) and with polarization spectra extracted for an additional number of viewing angles. Specifically, 17 and 21 extra-orientations were selected to properly sample the ejecta of the 2D D-DET and 3D N100-DDT model, respectively. Results of these simulations will be presented in Section 5.2.

[2] The choice of restricting our study to the $x$-$z$ plane is sufficient since the model has azimuthal symmetry about the $z$ axis.

### 3.2 Polarization decomposition and MC noise

An important drawback of MC simulations is their stochastic nature: MC noise in our extracted spectra can become sufficiently large to make the identification of real features challenging. This is particularly critical for the explosion models presented in this study since the modest asphericities of their ejecta (see Fig. 1 and discussion in Section 2) are expected to yield low values of polarization ($\lesssim 1$ per cent). Here we outline the choices we make to present our results and discriminate between intrinsic polarization signals and MC noise in this paper.

Polarization is sometimes represented in terms of the Stokes parameters $Q$ and $U$, sometimes in terms of degree of polarization $P = \sqrt{Q^2 + U^2}/I$ and polarization angle $\chi$ (derived from $\tan 2\chi = U/Q$). When dealing with low signal-to-noise levels, however, the former representation is usually preferred as $P$ is known to suffer from the so-called polarization bias (see e.g. Patat & Romaniello 2006, and references therein). Specifically, every contribution to $Q$ and $U$ in our simulations will be distributed around the true value $\bar{Q}$ and $\bar{U}$ because of MC noise fluctuations. In the presence of small signals, $Q$ and $U$ contributions can assume both positive and negative values. Given that the polarization percentage $P$ is defined positive, however, negative $Q$ and $U$ contributions will add only in the positive direction leading to a systematic overestimate of the true value $\bar{P}$.

Therefore, in this paper we will initially work in terms of the Stokes parameters as these do not suffer from the polarization bias. Following Leonard et al. (2001) and Wang et al. (2003), we also introduce a new set of Stokes parameters $Q_{\rm ROT}$ and $U_{\rm ROT}$ by rotating $Q$ and $U$ by a given angle $\alpha$ that brings the strongest polarization signal along $Q_{\rm ROT}$:

$$\begin{cases} Q_{\rm ROT} = Q\cos\alpha - U\sin\alpha \\ U_{\rm ROT} = Q\sin\alpha + U\cos\alpha \end{cases} . \tag{1}$$

Specifically:

- for the 2D D-DET model, we exploit the axial symmetry of the explosion and plot $Q$ as $Q_{\rm ROT}$ and $U$ as $U_{\rm ROT}$ (i.e. $\alpha = 0$). Thanks to the azimuthal symmetry around the $z$-axis, $Q_{\rm ROT}$ is expected to contain *all* the polarization signal, while $U_{\rm ROT}$ should be consistent with zero (within the MC noise level, see below);
- for the 3D N100-DDT model, we identify $\alpha$ via a weighted least-squared fitting of a straight line in the $Q/U$ plane. After the rotation, $Q_{\rm ROT}$ is expected to contain *most of* the polarization signal, while $U_{\rm ROT}$ to be reflective of deviations from a single-axis geometry (see also Wang & Wheeler 2008).

We will, however, prefer to use $P$ when discussing polarization light curves in Section 4.3 (as the polarization bias is much less important there) and when comparing our models with data in Section 5 (as the comparison is more straightforward in terms of absolute percentage levels and this representation has been widely used in previous studies).

In this paper we estimate MC noise levels by exploiting the axial symmetry of the 2D D-DET model. Owing to the symmetry about the $z$-axis, no intrinsic polarization is expected in the $U_{\rm ROT}$ spectrum for this model. Deviations from zero in the $U_{\rm ROT}$ spectrum are instead associated with

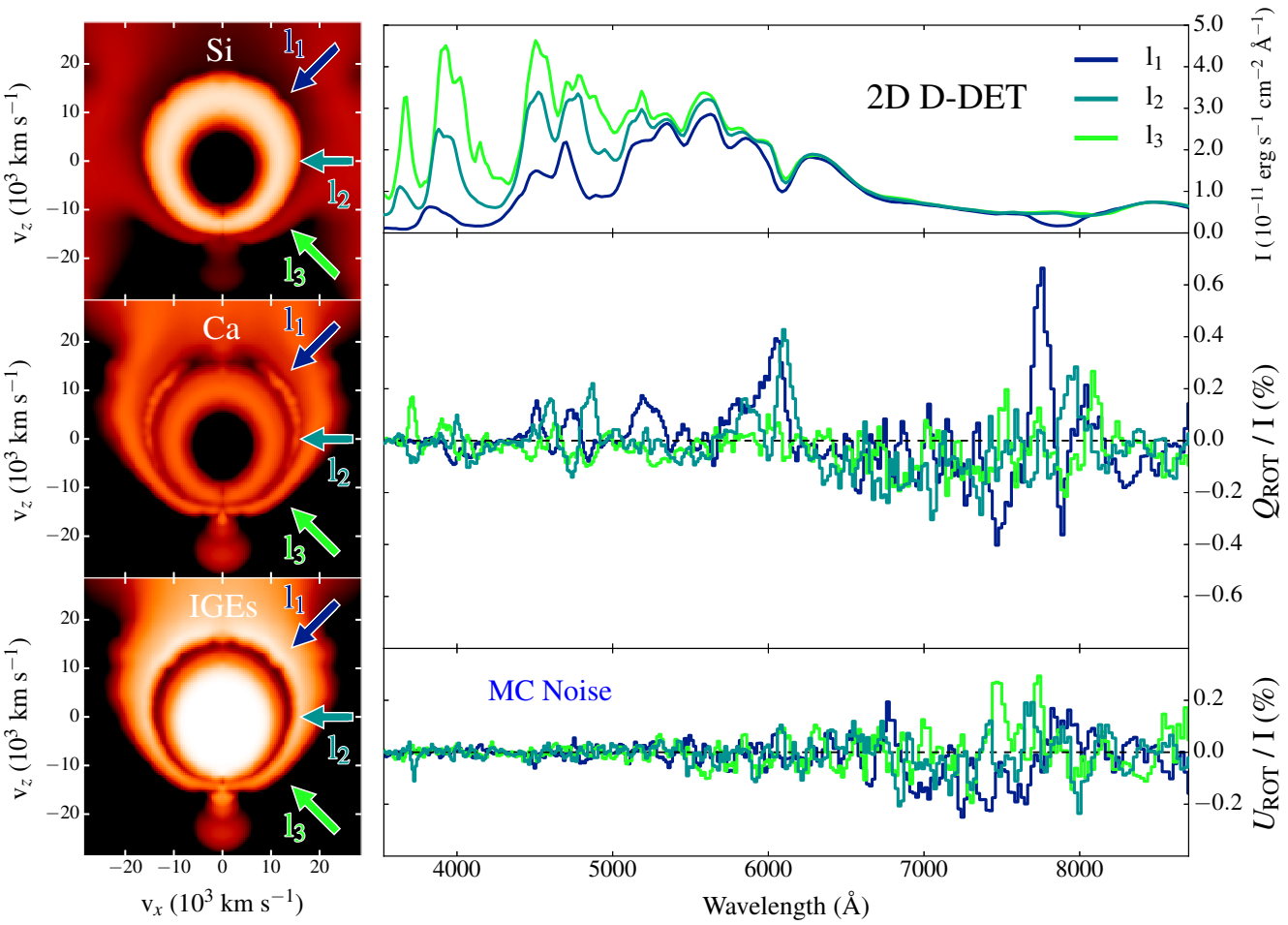


**Figure 2.** *Left-hand panels.* Orientations of the three observers selected for the D-DET model ($\boldsymbol{l_1}$, $\boldsymbol{l_2}$ and $\boldsymbol{l_3}$) with respect to the ejecta composition. The mass fractions of silicon (top), calcium (middle) and IGEs (bottom) are represented using the same colour scale of Fig. 1. *Right-hand panels.* Flux (top) and polarization $Q_{\rm ROT}$ (middle) spectra at 18.5 d after explosion ($B-$band maximum light) for the three chosen viewing angles. Polarization $U_{\rm ROT}$ spectra are reported in the bottom panel and provide proxies for the MC noise levels in the $Q_{\rm ROT}$ spectra (see discussion in Section 3.2). Polarization spectra are Savitzky-Golay filtered using a first-order polynomial and a window of 3 pixels ($\sim$ 50 Å) for clarity. The model flux is given for a distance of 1 Mpc.

statistical fluctuations and can be used as a convenient proxy for the MC noise in the $Q_{\rm ROT}$ spectrum. Given that both explosion models are investigated with the same number of MC quanta $N_{\rm q}$, we assume their statistical fluctuations to be comparable. Therefore, we also consider the $U_{\rm ROT}$ spectra for the 2D D-DET model as representative of the MC noise in the $Q_{\rm ROT}$ and $U_{\rm ROT}$ spectra of the 3D N100-DDT model.

## 4 SYNTHETIC OBSERVABLES

In this section, we present synthetic observables for the D-DET and N100-DDT models introduced in Section 2. For the N100-DDT model, qualitatively similar conclusions are found for the five different orientations and thus we present results for only three viewing angles ($\boldsymbol{n_1} - \boldsymbol{n_3}$) for simplicity; the calculations for the other two observer orientations will be included in the comparison with data in Section 5, however. We discuss flux and polarization spectra around maximum light in Section 4.1, illustrate how asymmetries in the element distribution are linked to specific polarization features in Section 4.2 and finally study the temporal evolution of the polarization signal in Section 4.3.

### 4.1 Polarization around maximum light

#### *4.1.1 2D D-DET model*

In Fig. 2 we show flux and polarization spectra for the selected D-DET model orientations $\boldsymbol{l_1}$ (north), $\boldsymbol{l_2}$ (equator) and $\boldsymbol{l_3}$ (south). Spectra are reported at $t^{\rm B}_{\rm max}$ = 18.5 d after explosion, that is around $B-$band maximum light for all the observers. As described by Kromer et al. (2010), the asymmetries in the ejecta (see Fig. 1) translate into strongly viewing-angle dependent flux spectra. Compared to packets escaping in the southern hemisphere (along $\boldsymbol{l_3}$), those on the opposite side (along $\boldsymbol{l_1}$) have to travel through a more extended layer of IGEs and are therefore more likely to be absorbed and reemitted at longer wavelengths. This effect leads to a much redder spectrum for the orientation in the

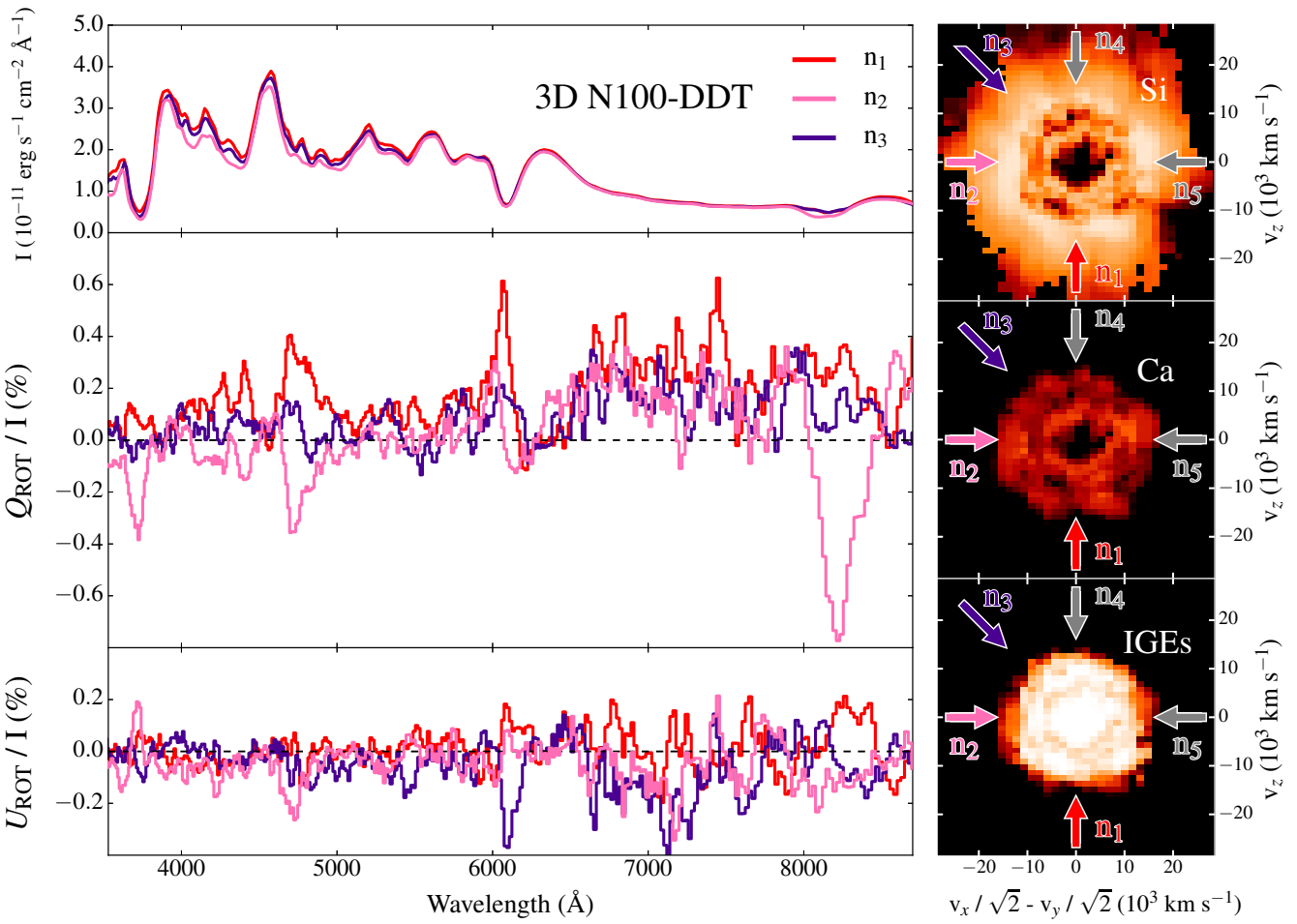


**Figure 3.** *Left-hand panels.* Flux (top) and polarization $Q_{\rm ROT}$ (middle) spectra extracted for the N100-DDT model at 17 d after explosion ($B-$band maximum light) along the $\boldsymbol{n_1}$, $\boldsymbol{n_2}$ and $\boldsymbol{n_3}$ orientations. Polarization $U_{\rm ROT}$ spectra are reported in the bottom panel and reflect deviations from a single-axis geometry (see discussion in Section 3.2). $U_{\rm ROT}$ spectra in the D-DET model (see bottom panel of Fig. 2) provide estimates of the MC noise levels in both $Q_{\rm ROT}$ and $U_{\rm ROT}$. Polarization spectra are Savitzky-Golay filtered using a first-order polynomial and a window of 3 pixels ($\sim$ 50 Å) for clarity. The model flux is given for a distance of 1 Mpc. *Right-hand panels.* Orientations of the five observers selected for the N100-DDT model ($\boldsymbol{n_1}-\boldsymbol{n_5}$) with respect to the ejecta composition. The mass fractions of silicon (top), calcium (middle) and IGEs (bottom) are represented using the same colour scale of Fig. 1.

northern hemisphere. Owing to the off-center ignition of the core (see Section 2), IMEs are also more abundant and distributed over a wider velocity range in the northern hemisphere. IME spectral features extracted along $\boldsymbol{l_1}$ are thus stronger and broader compared to those along $\boldsymbol{l_3}$ (see for instance the Si II $\lambda$6355 line and Ca II IR triplet). Intermediate spectral properties are found for the equatorial observer orientation ($\boldsymbol{l_2}$).

Polarization levels extracted for the three chosen observer orientations are relatively low ($|Q_{\rm ROT}| \lesssim 0.7$ per cent). Polarization signals throughout the spectrum are generally stronger for the fainter orientation ($\boldsymbol{l_1}$) and weaker for the brighter orientation ($\boldsymbol{l_3}$), although deviations from this behaviour are seen. We do, however, find similar degrees of polarization ($Q_{\rm ROT} \sim -0.1$ per cent, see also Section 4.3) for all observer orientations in the "pseudo-continuum" region 6500−7500 Å, a region usually assumed to be devoid of strong lines and thus reflective of the continuum level (Kasen et al. 2004; Leonard et al. 2005; Patat et al. 2009). Non-zero continuum polarization in SNe is representative of asymmetries in the underlying electron-scattering photosphere. Therefore, the extremely low levels found across the pseudo-continuum region 6500−7500 Å arise as a direct consequence of the overall spherical symmetry of the inner regions of the ejecta (velocities between $\sim$ 5000 and 15 000 km s$^{-1}$, see Fig. 1), from which most of the electron-scattered polarizing contributions originate (see Fig. 4).

Despite the small signal in the pseudo-continuum, the polarization increases at wavelengths corresponding to the absorption troughs of spectral lines. In the upper panels of Fig. 5, we report polarization spectra between 5000 and 8500 Å extracted along the $\boldsymbol{l_1}$ direction. Matches between spectral lines and polarization peaks are unambiguous above 5000 Å. The strongest polarization feature in this range is a peak of about 0.7 per cent around 7700 Å, which clearly corresponds to the Ca II IR

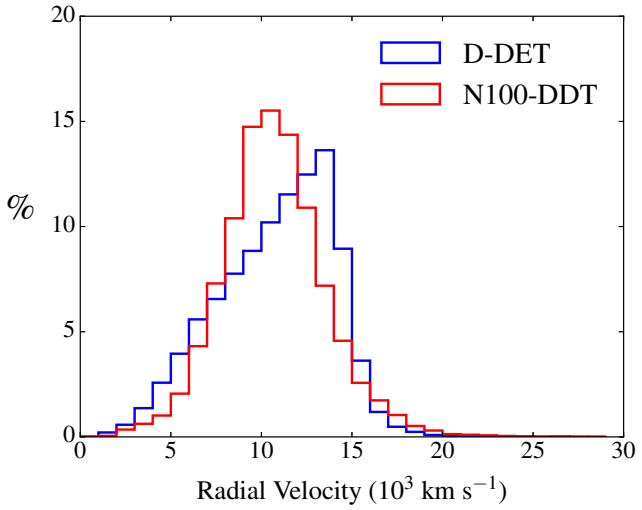


**Figure 4.** Region of last scattering for polarizing contributions. Distributions include radial velocities at the points where packets underwent a polarizing interaction (i.e. electron scattering) as last interaction before escaping towards the observer. $10^6$ packets have been used for both the D-DET (blue) and the N100-DDT (red) model.

triplet at high-velocities (v $\sim -26\,000$ km s$^{-1}$) and reflects the asymmetric distribution of calcium in the outer shell (but see also discussion in Section 4.2.1). Other peaks are instead found at lower velocities (between $-10\,000$ and $-13\,000$ km s$^{-1}$) and attributed to silicon and sulphur transitions in the outer layers of the core detonation. Compared to calcium, these elements are more spherically distributed and thus characterized by weaker polarization signatures ($|Q_{\rm ROT}| \lesssim 0.4$ per cent). Specifically, we find clear polarization signals for the Si II $\lambda$6355 line (see also Section 5.2), while smaller – and possibly null – signals are predicted for the S II $\lambda$5454, S II $\lambda$5640 and Si II $\lambda$5972 lines. A clear polarization feature is also seen around 7500 Å, with negative $Q_{\rm ROT}$ (i.e. 90° rotated from the rest of the features). In our simulations, this features can be attributed to a blend of O I $\lambda\lambda$7772, 7774, 7775 (hereafter O I $\lambda$7774), Si II $\lambda\lambda$7849, 7850 (Si II $\lambda$7849) and Mg II $\lambda\lambda$7877, 7896 (Mg II $\lambda$7887), with relative contributions that depend on orientation and epoch. The nature of this polarization spike and its 90° rotation from the rest of the features will be investigated in Section 4.2. With the exception of a polarization peak around 3700 Å, associated with the Si II $\lambda$3859 and/or Ca H and K features, identifications to individual transitions are not obvious below $\sim$ 5000 Å due to the strong line blending suffered by these blue regions.

#### *4.1.2 3D N100-DDT model*

In the top panel of Fig. 3 we show flux spectra for the N100-DDT model orientations $\boldsymbol{n_1}$, $\boldsymbol{n_2}$ and $\boldsymbol{n_3}$ at $t^{\rm B}_{\rm max} = 17$ d after explosion (around $B-$band maximum light for the three orientations). As shown in Fig. 1, the ejecta distribution in the N100-DDT model is rather spherical and does not have IGE material at very high velocities, in contrast to the D-DET model. Compared to the D-DET model, the N100-DDT model is therefore characterized by a much smaller viewing angle dependence in the flux spectra (Sim et al. 2013). One noticeable difference is found for the blue-shifted absorption component of the Ca II IR triplet, which is stronger when observed from an equatorial orientation $\boldsymbol{n_2}$. This can be understood by noting that the calcium distribution is not perfectly spherical (see right panels of Fig. 3) and offers higher opacities to packets escaping towards $\boldsymbol{n_2}$ compared to those escaping in the other two directions considered here.

The bottom panels of Fig. 3 show polarization spectra $Q_{\rm ROT}$ and $U_{\rm ROT}$ . By construction (see Section 3.2), the strongest polarization signal is carried by $Q_{\rm ROT}$ for all the viewing angles. However, as the original Stokes parameters are poorly described by a straight line in the $Q/U$ plane (see Fig. 6), some residual polarization is also found along $U_{\rm ROT}$. In particular, a simple comparison with the MC noise spectrum of the D-DET model (see Fig. 2) clearly confirms that polarization levels in the $U_{\rm ROT}$ spectra of the N100-DDT model can not be solely due to MC noise. The strongest deviations from a single-axis geometry are generally associated with spectral lines, as seen for instance across the Si II $\lambda$6355 feature in the $\boldsymbol{n_3}$ direction.

As in the flux spectrum, the largest line-of-sight variability in the polarization percentage level is found across the Ca H and K and Ca II IR triplet profiles. Compared to the other two orientations, the polarization signal along $\boldsymbol{n_2}$ is a factor of $\sim$ 3 stronger and reaches peak levels of $\sim$ 0.4 per cent and $\sim$ 0.8 per cent in the Ca H and K and Ca II IR triplet, respectively. Some viewing-angle variations are also observed for the Si II $\lambda$6355 line, but now the $\boldsymbol{n_2}$ orientation is associated with the weakest signal (0.3 per cent) and the $\boldsymbol{n_1}$ observer with the strongest (0.6 per cent).

The pseudo-continuum region 6500−7500 Å is characterized by polarization levels of about 0.2−0.3 per cent for all the orientations (see also Section 4.3). As shown in Fig. 5 for the $\boldsymbol{n_1}$ orientation, our synthetic spectropolarimetry in this spectral range contains a number of small peaks. Most of these, however, can be ascribed to statistical fluctuations in the simulations since deviations from the mean degree of polarization ($Q_{\rm ROT} \sim 0.3$ per cent) are typically smaller than the average MC noise level in this range ($\sim$ 0.2 per cent, see $U_{\rm ROT}$ in the D-DET model). This is verified in the lower panels of Fig. 5, where we plot a smoothed version of the $Q_{\rm ROT}$ spectrum. In the latter, pixel-to-pixel variations due to MC noise are suppressed, while real features are still visible (see e.g. the Si II $\lambda$6355 line). We note, however, that the peak around 7500 Å appears real and, as mentioned above for the D-DET model, is associated with O I $\lambda$7774, Si II $\lambda$7849 and Mg II $\lambda$7887. The nature of this feature will be investigated in the following section.

### 4.2 Linking polarization to the ejecta geometry

In this section, we will examine more closely how asymmetries in the element distribution are linked to individual polarization features. In particular, we focus on two examples. First, we investigate the link between the calcium distribution in the ejecta and the polarization signatures detected across the Ca II IR triplet profile. Second, we look at the oxygen, magnesium and silicon morphologies to understand which of these elements are responsible for the polarization features observed around 7500 Å (see Section 4.1). We frame

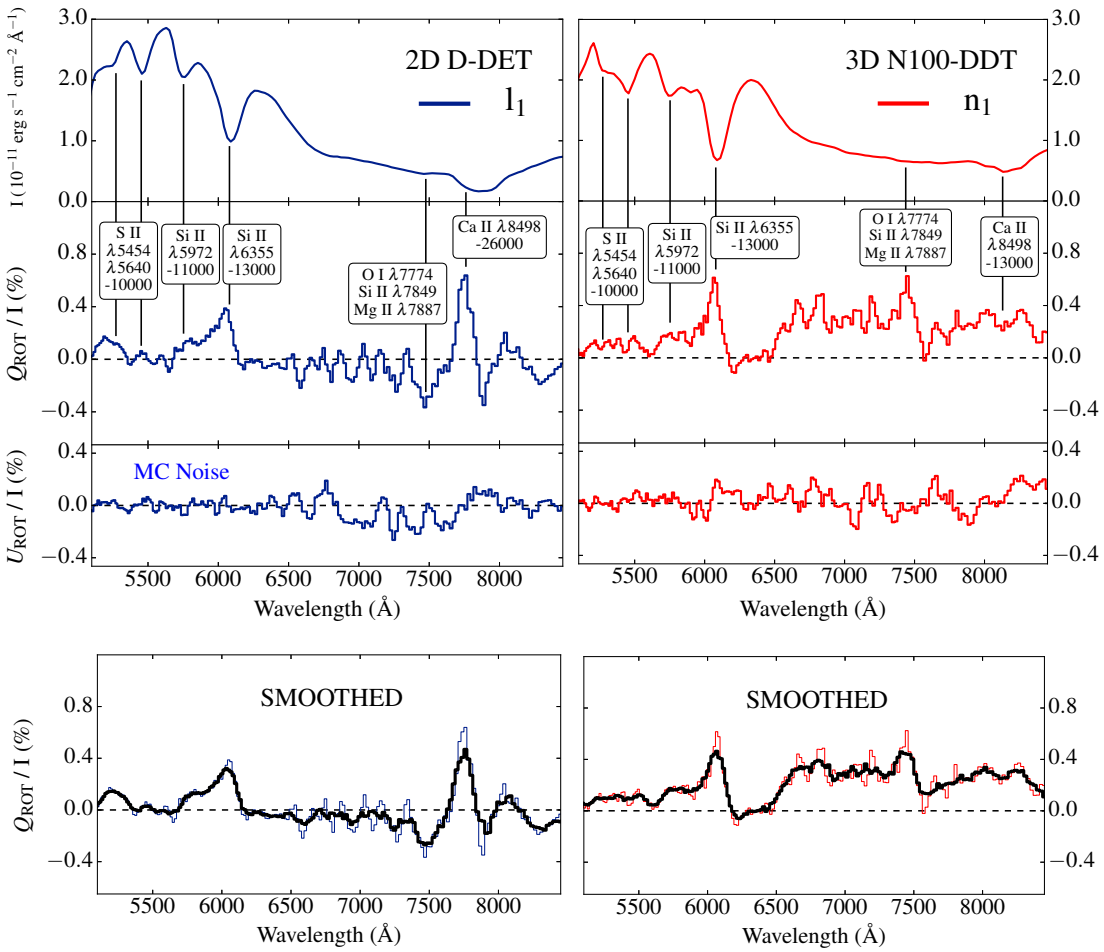


**Figure 5.** *Upper panels.* Identification of individual spectral transitions in the 5000−8500 Å wavelength region. Left-hand panels show flux and polarization spectra for the D-DET model viewed from $\boldsymbol{l_1}$, while right-hand panels spectra extracted for the N100-DDT model along $\boldsymbol{n_1}$. Spectra are the same as in Fig. 2 and Fig. 3. Signals in the 2D D-DET model $U_{\rm ROT}$ are only due to statistical fluctuations in the simulations and provide estimates of the MC noise levels in all the other polarization spectra (see Section 3.2). Vertical lines provide identifications of polarization peaks with spectral transitions. Rest-frame wavelength and blue-shifted velocity of each transition are reported in the corresponding label. Polarization spectra are Savitzky-Golay filtered using a first-order polynomial and a window of 3 pixels ($\sim$ 50 Å) for clarity. *Lower panels.* The same $Q_{\rm ROT}$ spectra reported in the upper panels, together with smoothed versions (black) using a Savitzky-Golay filter with a window of 7 pixels ($\sim$ 120 Å). No clear polarization feature is found between 6500 and 7300 Å.

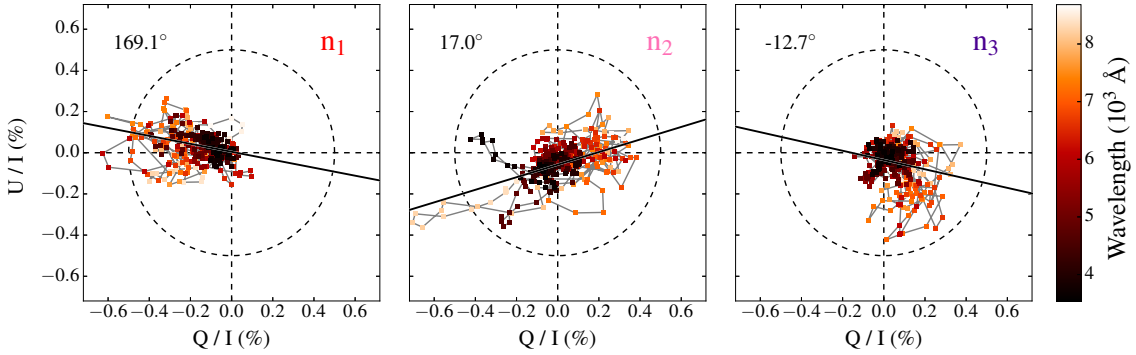


**Figure 6.** $Q/U$ planes for the N100-DDT model at maximum light as viewed from the $\boldsymbol{n_1}$ (left), $\boldsymbol{n_2}$ (middle) and $\boldsymbol{n_3}$ (right) directions. A weighted least-squares fitting to the data is performed for each orientation and the result plotted as a solid black line. The angles determined from the fitting and used to convert $Q$ and $U$ to the polarization spectra of Fig. 3 are also reported in each panel. Black circles mark polarization levels of 0.5 per cent. $Q$ and $U$ Stokes parameters are Savitzky-Golay filtered using a first-order polynomial and a window of 3 pixels ($\sim$ 50 Å) for clarity.

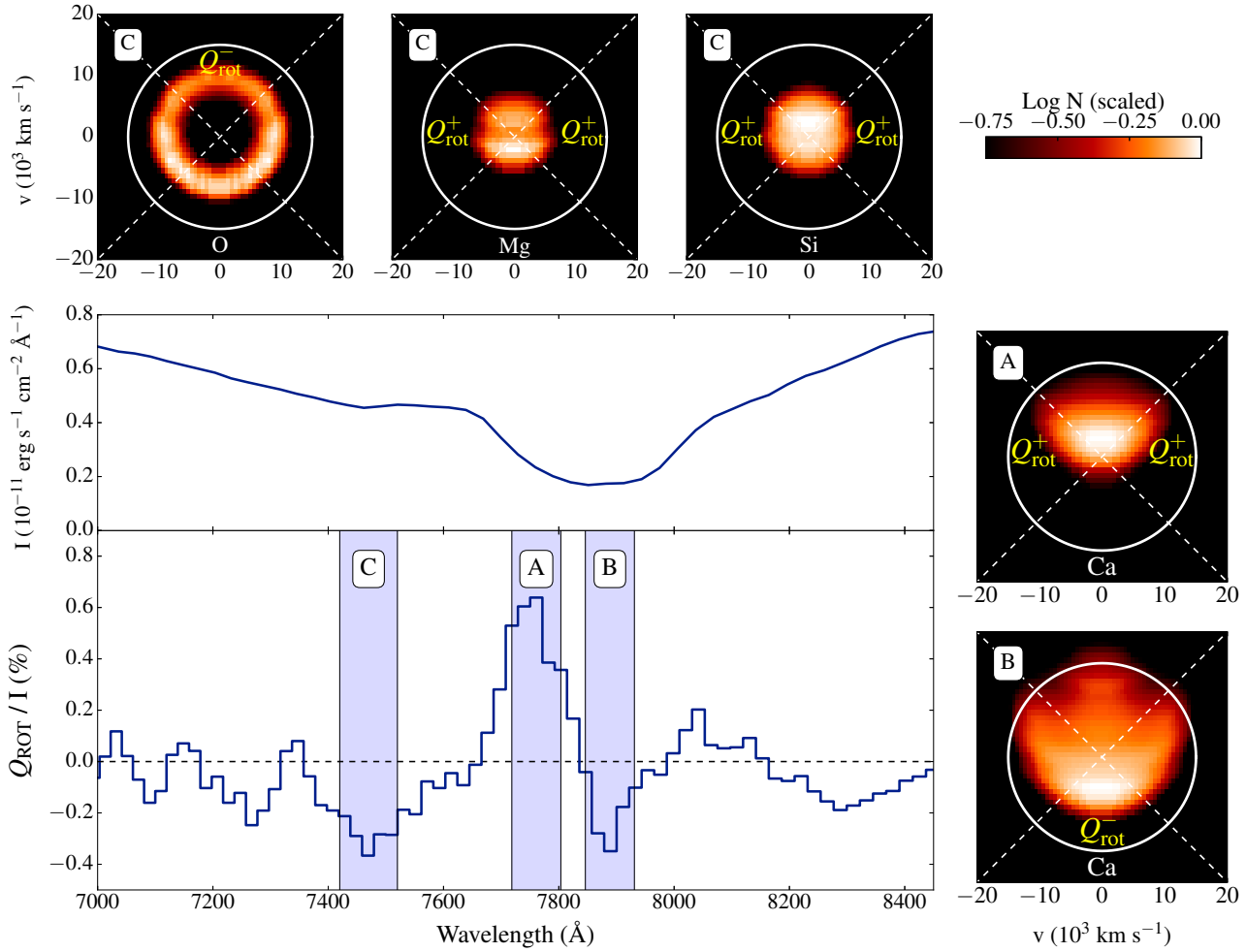


**Figure 7.** Colour maps of the oxygen, magnesium, silicon (top panels) and calcium (right panels) column densities $N$ calculated through the near-side hemisphere of the ejecta in the D-DET $\boldsymbol{l_1}$ direction. As shown by the grey areas in the $Q_{\rm ROT}$ spectrum (bottom-left panel), column densities in each map are integrated over different velocity ranges through the ejecta to enclose the polarization peaks in the Ca II IR triplet profile (map A and map B) and the feature around 7500 Å (map C). White circles mark a projected velocity of 15 000 km s$^{-1}$, within which most of the electron-scattering contributions originate (see Fig. 4). For each map, regions of the ejecta dominating the polarization signal are indicated with $Q^{+}_{\rm rot}$ or $Q^{-}_{\rm rot}$ if their contribution to $Q_{\rm ROT}$ is positive or negative, respectively. The column densities of each map are scaled by the maximum value. Due to the axi-symmetry of the D-DET model, maps display a left-right symmetry.

our discussion in terms of the physical picture in which polarization variations across spectral lines can be understood as resulting from partial covering of the electron-scattering photosphere caused by the asymmetric distributions of elements in the ejecta (see e.g. Kasen et al. 2003).

### *4.2.1 2D D-DET model*

As shown in Fig. 7, the polarization signature extracted across the Ca II IR triplet in the $\boldsymbol{l_1}$ direction is characterized by a transition from positive to negative $Q_{\rm ROT}$ levels at around 7830 Å (corresponding to velocities of about −23 500 km s$^{-1}$). This transition can be understood by inspecting the calcium distribution in the D-DET ejecta more closely. The colour maps in the right panels of Fig. 7 present column densities ($N$) for Ca calculated through the near-side hemisphere of the ejecta along the D-DET $\boldsymbol{l_1}$ direction. We first notice that the distribution of calcium at very high velocities (−26 000 km s$^{-1}$, map A) preferentially covers the top side of the ejecta as viewed from the $\boldsymbol{l_1}$ orientation. Most of the electron-scattered contributions from this side of the ejecta – mainly polarized in the negative $Q_{\rm ROT}$ direction – are thus absorbed by calcium and do not reach the observer. As a result, positive contributions from the left and right side of the ejecta dominate the signal and produce a polarization peak with $Q_{\rm ROT} > 0$ in the Ca II IR triplet profile. If we now move deeper into the ejecta (−21 500 km s$^{-1}$, map B), we notice that here the top, left and right sides are preferentially obscured by calcium. Hence, packets are more likely to escape from the bottom side of the ejecta and bias the polarization signal towards negative values ($Q_{\rm ROT} < 0$) in the Ca II IR profile.

As pointed out in Section 4.1.1, the spectrum extracted along the $\boldsymbol{l_1}$ orientation is characterized by a clear polar-

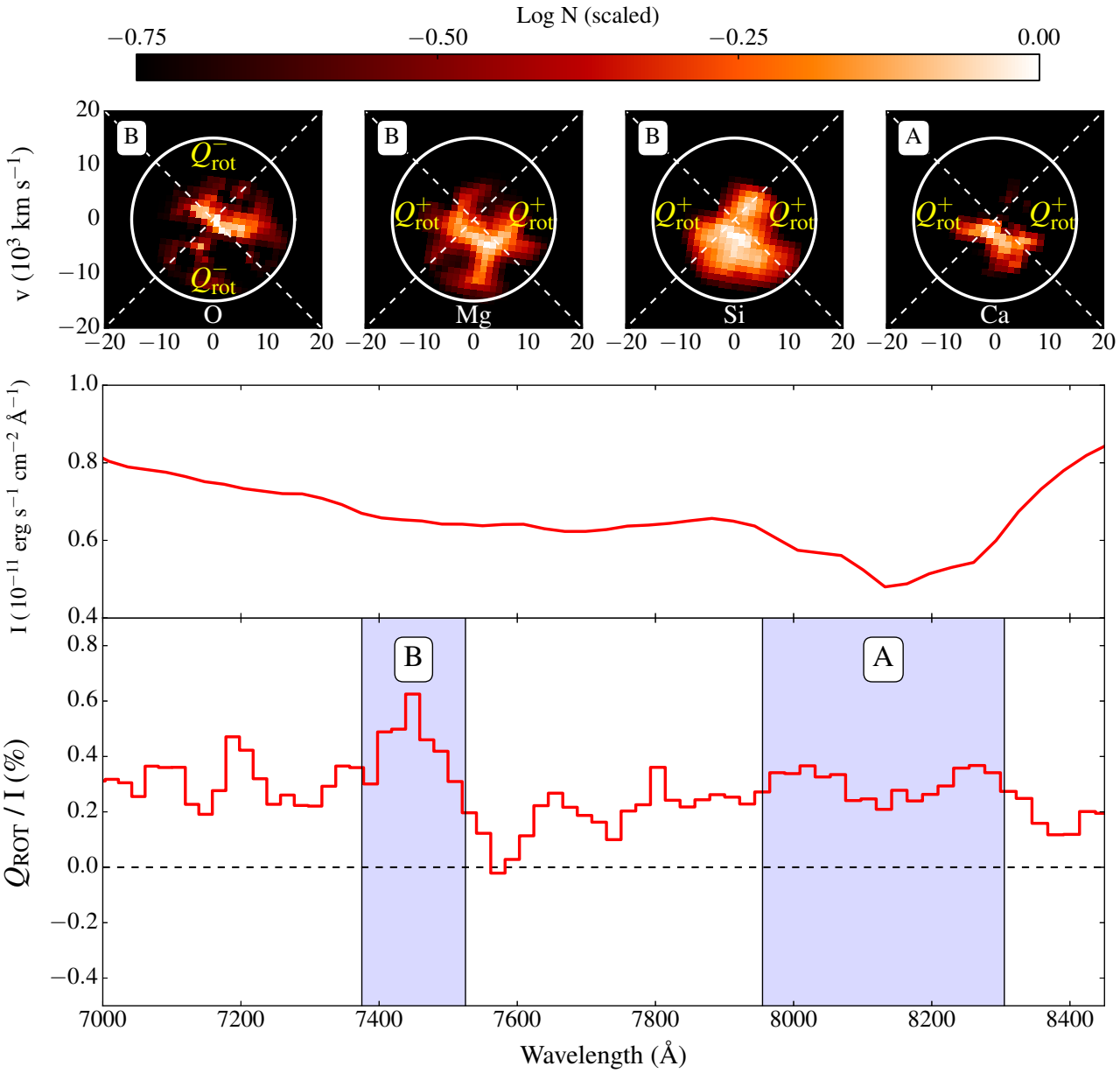


**Figure 8.** Same as Fig. 7, but for the N100-DDT viewed along the $\boldsymbol{n_1}$ direction. Colour maps have been rotated of $\alpha_{\rm rot}/2 = 84.5°$ (see left panel of Fig. 6) in the clockwise direction to account for the transformation of $Q$ and $U$ to $Q_{\rm ROT}$ and $U_{\rm ROT}$ (see Section 3.2).

ization feature around 7500 Å. This feature is polarized in the negative $Q_{\rm ROT}$ direction, meaning that its polarization angle is 90° rotated from most of the other features in the spectrum (e.g. the Si II $\lambda$6355 line, see Fig. 5). Three spectral transitions can be responsible for the variation in polarization across this spectral region: O I $\lambda$7774, Si II $\lambda$7849 or Mg II $\lambda$7887. As shown in the upper panels of Fig. 7, two distinct behaviours are seen in the distributions of oxygen, magnesium and silicon: the asymmetric distributions of magnesium and silicon will cause positive contributions from the left and right sides of the ejecta to dominate the polarization signal[3]. On the other hand, the distribution of oxygen will favour negative contributions (from the top side of the ejecta) dominating the signal. Therefore – although all the three aforementioned transitions are expected to affect the degree of polarization to some extent – we suggest that the polarization signal extracted around 7500 Å in the $\boldsymbol{l_1}$ direction is dominated by O I $\lambda$7774. This identification explains why we see a 90° rotation between the feature around 7500 Å and the silicon lines (e.g. Si II $\lambda$5972 and Si II $\lambda$6355, see Fig. 5).

[3] Note that this is consistent with the positive signals detected across the silicon lines, see Fig. 5.

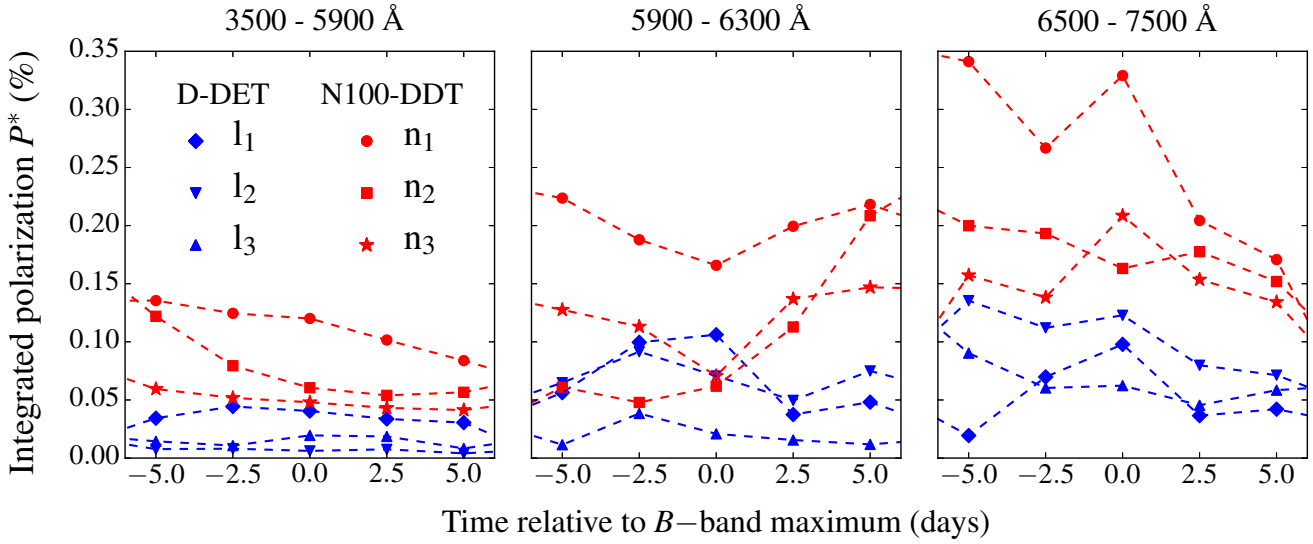


**Figure 9.** Polarization light curves between −5 and +5 d relative to $B-$band maximum light calculated in three different wavelength ranges: 3500−5900 Å (left-hand panel,"blue" range), 5900−6300 Å (middle panel, around the Si II $\lambda$6355 line) and 6500−7500 Å (right-hand panel, pseudo-continuum range). MC noise error bars are $\sim$ 0.001, 0.013 and 0.029 per cent in the left-hand, middle and right-hand panel, respectively.

#### *4.2.2 3D N100-DDT model*

As shown in the bottom panels of Fig. 8, positive $Q_{\rm ROT}$ polarization levels are detected across the Ca II IR profile for the N100-DDT $\boldsymbol{n_1}$ direction. This is readily understood by looking at the distribution of calcium in the ejecta of the N100-DDT model (map A, top right panel of Fig. 8). When viewed from the $\boldsymbol{n_1}$ observer orientation, the asymmetric distribution of calcium offers higher opacities to packets escaping towards the observer from the bottom side of the ejecta. As a result, the polarization signal across the Ca II IR profile is dominated by contributions coming from the left and right sides and thus biased towards positive values.

As mentioned in Section 4.1.2, the polarization spectrum extracted for the N100-DDT model is characterized by a signature in the wavelength region occupied by the O I $\lambda$7774, Si II $\lambda$7849 and Mg II $\lambda$7887 lines. Specifically, this feature is polarized in the positive $Q_{\rm ROT}$ direction when viewed from the $\boldsymbol{n_1}$ direction. As shown in the top panels of Fig. 8 (maps B), magnesium and silicon column densities extracted along $\boldsymbol{n_1}$ are higher on the bottom side of the ejecta, thus favouring positive contributions to dominate the $Q_{\rm ROT}$ polarization signal. In contrast, oxygen preferentially absorbs packets from the right side of the ejecta and thus biases the $Q_{\rm ROT}$ polarization signal towards negative values. Based on this analysis, we therefore suggest that – unlike what is seen for the D-DET model – the polarization signal across the 7500 Å feature is dominated by Si II $\lambda$7849 and Mg II $\lambda$7887. Although the contribution of O I $\lambda$7774 appears not to be dominant in this case – i.e. around maximum light and towards the $\boldsymbol{n_1}$ observer orientation – we note that the same might not be true for different directions and at different epochs (see Section 5.3).

### 4.3 Polarization light curves

In this section, we investigate the temporal evolution of polarization for the D-DET and N100-DDT models. Following Bulla et al. (2015), we calculate intensity ($I^*$) and polarization ($Q_{\rm ROT}{}^*$ and $U_{\rm ROT}{}^*$) light curves by integrating the flux and polarization spectra over selected wavelength ranges $[\lambda_1, \lambda_2]$:

$$\begin{bmatrix} I^*(t) \\ Q_{\rm ROT}{}^*(t) \\ U_{\rm ROT}{}^*(t) \end{bmatrix} = \int_{\lambda_1}^{\lambda_2} \begin{bmatrix} I(\lambda,t) \\ Q_{\rm ROT}(\lambda,t) \\ U_{\rm ROT}(\lambda,t) \end{bmatrix} \, {\rm d}\lambda \; . \quad (2)$$

Specifically, we focus our attention on three spectral regions: from 3500 to 5900 Å ("blue" range), from 5900 to 6300 Å (Si II $\lambda$6355 range) and from 6500 to 7500 Å (pseudo-continuum range, see above). Given that MC noise levels integrated in these three wavelength ranges are low (0.001, 0.013 and 0.029 per cent, respectively), polarization bias (see Section 3.2) is less an issue here. Therefore, we restrict our discussion to the time evolution of the integrated polarization percentage $P^*$ defined as

$$P^*(t) = \frac{\sqrt{Q_{\rm ROT}{}^*(t)^2 + U_{\rm ROT}{}^*(t)^2}}{I^*(t)} \; . \quad (3)$$

Fig. 9 reports $P^*$ around $B-$band maximum light for the D-DET and N100-DDT models in the three selected ranges.

First, we notice that polarization levels for the D-DET model are generally lower in all ranges and at all epochs compared to those found for the N100-DDT model. Second, we find pseudo-continuum polarization levels for both models (right panel of Fig. 9) to vary in the range between 0.05 and 0.3 per cent, in good agreement with spectropolarimetric observations of SNe Ia (Wang & Wheeler 2008). Finally, both models are characterized by an increase in the degree of polarization with wavelength, a behaviour that can not be ascribed solely to MC noise growing from blue to red regions of the spectra (see above). As proposed

by Wang et al. (1997) and observed in several SNe Ia, this rise in polarization towards the red occurs as a result of the decreasing contribution of lines to the opacity[4]. In our simulations the fraction of escaping packets that had a line interaction as their last event are $\sim 75$, 50 and 30 per cent in the 3500−5900 Å, 5900−6300 Å and 6500−7500 Å ranges, respectively.

The low MC noise levels in the integrated quantities defined above allows us to study the polarization evolution around maximum. In all the spectral ranges, we find polarization levels for the D-DET model to reach their peak between 0 − 5 d before $B-$band maximum light, and to decrease thereafter. This behaviour is consistent with what is seen in SNe Ia and usually ascribed to the photosphere transitioning from asymmetric outer ejecta to more spherical inner regions (Wang & Wheeler 2008). Qualitatively similar results are found for the N100-DDT model, although $P^*$ across the Si II $\lambda$6355 profile continues to increase after maximum light, in this case (middle panel in Fig. 9).

## 5 COMPARISON WITH OBSERVATIONS

Here we compare our model spectra with observational data of normal SNe Ia. In Section 5.1 we present comparisons between full polarization spectra predicted by our models and those observed in normal SNe Ia. In Section 5.2, Section 5.3 and Section 5.4 we then focus our attention on the polarization signals across the Si II $\lambda$6355 line, the O I / Si II / Mg II feature around 7500 Å and the Ca II IR profile, respectively. Polarization values $P$ are used throughout this section, as has been common practice in previous studies including those that present the observational work to which we will compare (see also Section 3.2).

### 5.1 Comparison with SN Ia polarization spectra

In the following we compare flux and polarization spectra predicted for the D-DET and N100-DDT model with data of three well-studied SNe Ia: SN 2012fr, SN 2001el and SN 2004dt. These supernovae are selected as they have been observed in polarization at multiple epochs and with high spectral signal-to-noise ratio. In addition, the polarization range spanned by these objects encompasses the distribution observed for normal SNe Ia, going from the rather low levels observed for SN 2012fr to a high degree of polarization in SN 2004dt. Unless otherwise stated, we present synthetic spectra for the two orientations (one for the D-DET and one for the N100-DDT model) that provide best matches with observed flux and polarization spectra. We note, however, that spectra in better agreement with observations might be found for viewing angles not investigated in this study.

[4] Line scattering in SNe is usually assumed to depolarize the incoming radiation. Although resonance line scattering can lead to a polarization contribution (Hamilton 1947), the latter is typically lower than that from electron scattering and thus usually considered as a second-order effect (Jeffery 1989, 1991).

#### *5.1.1 SN 2012fr*

SN 2012fr was observed in polarization using the Focal Reducer and low dispersion Spectrograph (FORS1) at the ESO Very Large Telescope (VLT). Polarization levels were found to be generally very small ($\sim 0.1$ per cent in the pseudo-continuum range), although higher signals of $\sim 0.5-0.6$ per cent were detected across the Si II $\lambda$6355 and Ca II IR triplet features (Maund et al. 2013). In particular, a clear transition from high- (pre-maximum) to low- (post-maximum) velocity components was observed in the calcium profile. In Fig. 10, we show spectropolarimetric data of SN 2012fr at −5 and +2 d relative to $B-$band maximum together with synthetic spectra extracted for the D-DET and N100-DDT models at the same epochs. The best match between predicted and observed spectra is found for the D-DET $\boldsymbol{l_2}$ (upper panels) and N100-DDT $\boldsymbol{n_3}$ (lower panels) orientations.

There is a remarkably good match between the D-DET model and SN 2012fr at both epochs. Flux spectra of SN 2012fr are reproduced rather well by this model, both in terms of spectral shapes and velocities. The agreement is particularly good at 5 d before maximum, although we note two important discrepancies: the flux spectrum is too red and the velocity of Ca II IR triplet too low in our simulations. As discussed by Kromer et al. (2010), the red colour can be attributed to the composition of the burning yields in the outer shell. Specifically, the moderate amount of IGEs produced in the helium shell (see Fig. 1) leads to strong line blanketing in the blue spectral regions and flux redistribution to redder wavelengths (see also discussion in Section 4.1.1). The discrepancy in the velocity of the Ca II IR triplet is directly related to the specific distribution of calcium in the outer regions of the D-DET ejecta. Velocities of $\sim 17\,000$ km s$^{-1}$ measured in the synthetic profile are consistent with the calcium opacity predicted along the $\boldsymbol{l_2}$ orientation (see Fig. 1), but too small to reproduce those observed in the high-velocity features of SN 2012fr ($\sim 20\,000$ km s$^{-1}$, but see also Section 5.4).

The agreement between the D-DET model and observations is even more striking in terms of polarization. The match in the pseudo-continuum range (6500−7500 Å) and in the bluer regions of the spectra ($\lesssim 6000$ Å) is remarkable both pre- and post-maximum. In addition, the degrees of polarization observed across the Si II $\lambda$6355 line are nearly identical to those predicted by the D-DET model at −5 ($\sim 0.3$ per cent) and +2 ($\sim 0.4$ per cent) d relative to maximum. In contrast, we notice a poor match between model and data for the only other feature clearly detected in SN 2012fr, the Ca II IR triplet. While the calcium profile in SN 2012fr is characterized by a transition from a high-velocity component to three distinct low-velocity components, our model predicts a fairly strong and broad feature 5 d before maximum that almost disappears a week after. We note, however, that since the model fails to provide a convincing match to the Ca IR triplet in the flux spectrum (see above), it is not surprising that the match in polarization across this feature is also relatively poor.

As shown in the bottom panels of Fig. 10, the degree of polarization predicted for the N100-DDT model is broadly consistent with the levels observed in SN 2012fr. The polarization signals in the blue part of the spectrum

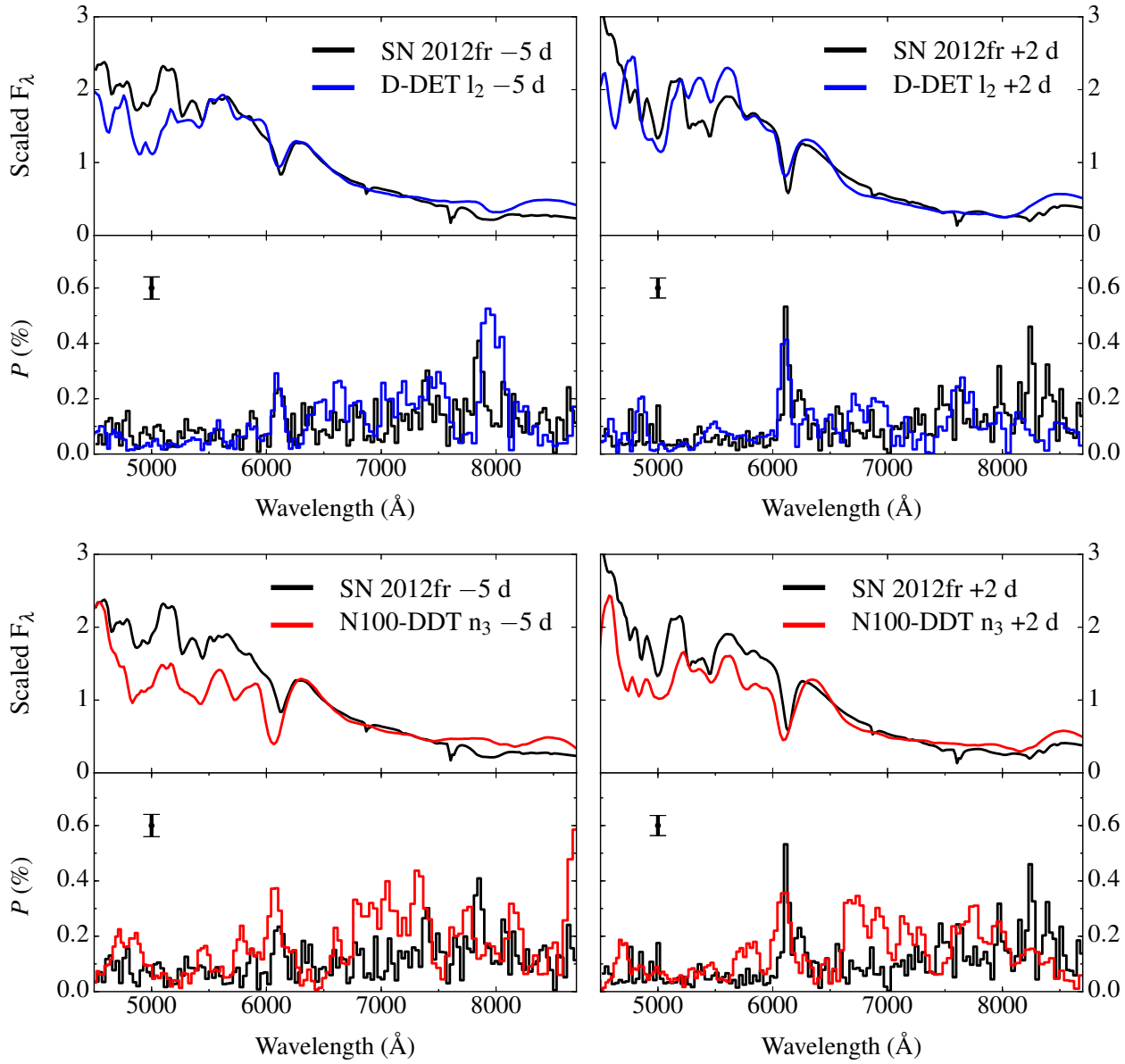


**Figure 10.** Flux and polarization spectra predicted for the D-DET (upper panels, blue lines) and N100-DDT (lower panels, red lines) models viewed from the $\boldsymbol{l_2} = (1, 0, 0)$ and $\boldsymbol{n_3} = (-1/2, 1/2, 1/\sqrt{2})$ orientations, respectively. Spectra are reported at −5 (left-hand panels) and +2 (right-hand panels) d relative to $B-$band maximum light. For comparison, black lines show observed spectra of SN 2012fr at the same epochs after correction for the interstellar polarization component ($\sim$ 0.24 per cent; Maund et al. 2013). Black bars mark the averaged errors in the observed polarization spectra. Both synthetic and observed flux spectra have been normalized to their values at 6500 Å for illustrative purposes.

and across the Si II $\lambda$6355 profile agree reasonably well with the data. However, we see larger discrepancies compared to those found in the D-DET case. First, the model predicts velocities along $\boldsymbol{n_3}$ that are typically higher than those observed (e.g. 30 per cent larger for the Si II $\lambda$6355 profile 5 d before maximum). Second, velocities for the calcium IR triplet ($\sim 13\,000$ km s$^{-1}$) are definitely too low to account for the high-velocity component observed in SN 2012fr (see also Section 5.4). Finally, the 6500−7500 Å pseudo-continuum range in the N100-DDT model spectrum is too highly polarized ($\sim$ 0.3 per cent) at both epochs to match the small signal of $\sim$ 0.1 per cent detected in SN 2012fr.

### *5.1.2 SN 2001el*

Spectropolarimetric observations of SN 2001el were triggered with FORS1 at ESO VLT. A polarization signal of $\sim$ 0.2−0.3 per cent – typical for the bulk of normal SN Ia events – was detected in the pseudo-continuum range (Wang et al. 2003). Two distinct components were clearly visible in the Ca II IR triplet: a significantly polarized ($\sim$ 0.7 per cent) high-velocity component and a distinct low-velocity component polarized at $\sim$ 0.2−0.3 per cent level. In Fig. 11, we compare observations of SN 2001el at −7, −2 and +7 d relative to $B-$band maximum with synthetic spectra extracted

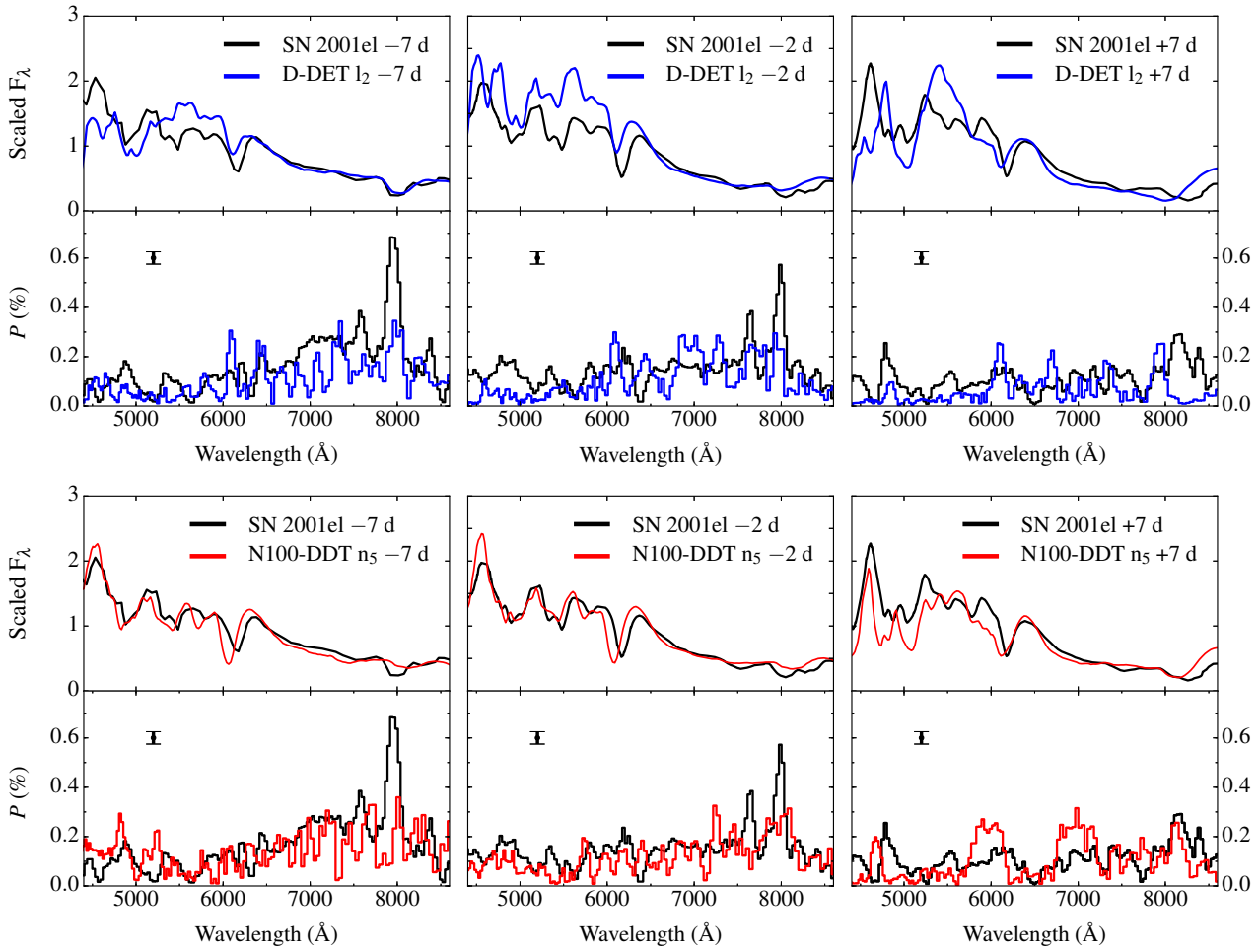


**Figure 11.** Flux and polarization spectra predicted for the D-DET (upper panels, blue lines) and N100-DDT (lower panels, red lines) models viewed from the $\boldsymbol{l_2} = (1, 0, 0)$ and $\boldsymbol{n_5} = (1/\sqrt{2}, -1/\sqrt{2}, 0)$ directions, respectively. Spectra are reported at −7 (left-hand panels), −2 (middle panels) and +7 (right-hand panels) d relative to $B-$band maximum light. For comparison, black lines show observed spectra of SN 2001el at the same epochs after correction for the interstellar polarization component ($\sim$ 0.6 per cent; Wang et al. 2003). Black bars mark the averaged errors in the observed polarization spectra. Both synthetic and observed flux spectra have been normalized to their values at 6500 Å for illustrative purposes.

for the D-DET (upper panels) and N100-DDT (lower panels) model at the same epochs. Specifically, we report the best matches found in each case, which are for the D-DET $\boldsymbol{l_2}$ and the N100-DDT $\boldsymbol{n_5}$ orientations.

Spectra extracted for the D-DET model along the equatorial $\boldsymbol{l_2}$ orientation are broadly consistent with those observed in SN 2001el. Polarization levels extracted in the pseudo-continuum region and across the Si II $\lambda$6355 profile are in good agreement with data, although velocities in the synthetic spectra are slightly larger than those observed. The most striking difference, however, concerns the Ca II IR triplet region. The calcium distribution in the outer shell of the D-DET model (see Fig. 1) is able to reproduce the high-velocity component seen in SN 2001el, but is not sufficiently asymmetric to explain the relatively high polarization level of 0.6−0.7 per cent observed. In this respect, it is worth noting that such strong polarization signals are predicted – at least around maximum – for the $\boldsymbol{l_1}$ orientation of the D-DET model (see for instance Fig. 2). However, this orientation is characterized by (i) spectra that are much too red and by (ii) a calcium line that is too strong and too fast to match the observations (see discussion in Section 5.4).

Spectra extracted for the N100-DDT model along $\boldsymbol{n_5}$ agree reasonably well with data of SN 2001el, although we again notice systematically larger velocities in the model. The match is particularly good before maximum light, with the predicted spectral color (see also Röpke et al. 2012) and degrees of polarization found to be consistent with observations. As in the D-DET model, however, the region around the Ca II IR triplet is poorly reproduced by the N100-DDT model. Here, the polarization signal is a factor of $\sim$ 2 smaller than that observed. Furthermore, the velocity is also too slow to reproduce the high-velocity component seen in SN 2001el before maximum.

### *5.1.3 SN 2004dt*

Spectropolarimetric observations of SN 2004dt were acquired with FORS1 at ESO VLT about a week before maximum (Wang et al. 2006) and with the Shane tele-

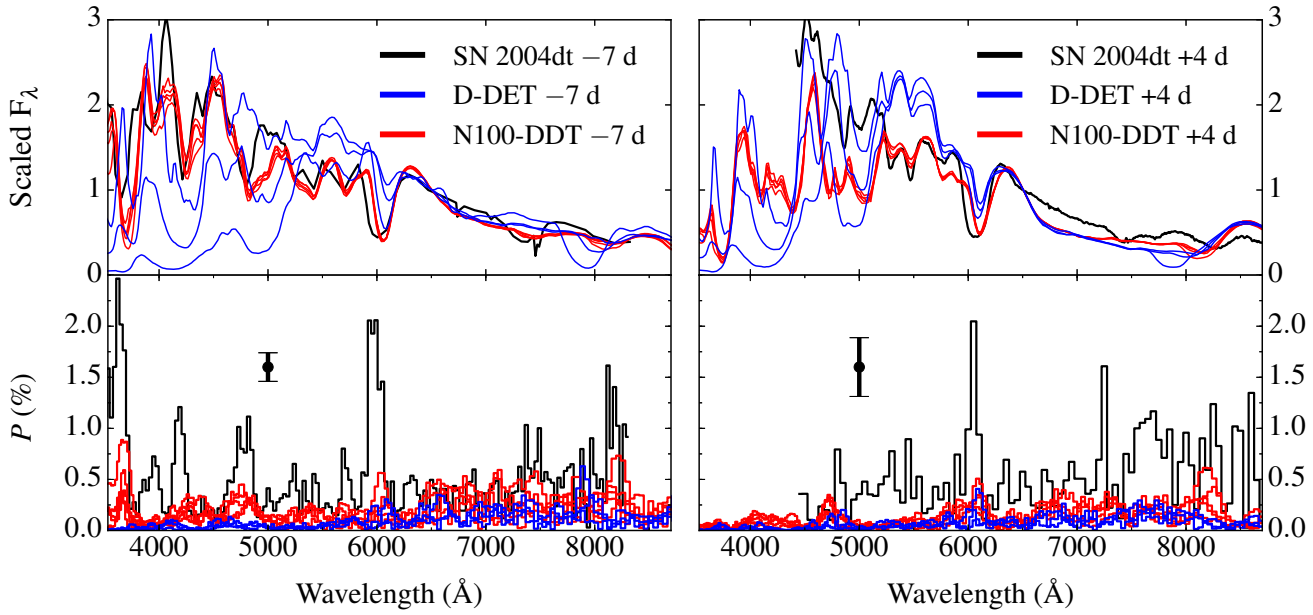


**Figure 12.** Flux (top) and polarization (bottom) spectra predicted for the D-DET (three blue lines) and the N100-DDT (five red lines) models for all the high signal-to-noise calculation orientations investigated in this paper. Spectra are reported at −7 (left-hand panels) and +4 (right-hand panels) d relative to $B-$band maximum. For comparison, black lines show observed spectra of SN 2004dt at the same epochs after correction for the interstellar polarization component ($\sim$ 0.28 per cent; Leonard et al. 2005; Wang et al. 2006). Black bars mark the averaged errors in the observed polarization spectra. Both synthetic and observed flux spectra have been normalized to their values at 6500 Å for illustrative purposes.

scope at Lick Observatory 4 d after maximum (Leonard et al. 2005). Except for the pseudo-continuum range, where degrees of polarization typical of normal SNe Ia ($\sim 0.3-0.4$ per cent) were detected, SN 2004dt displayed unusual polarization properties. Together with a very strong ($\sim 2-2.5$ per cent) peak around 3650 Å, several features polarized at $\sim$ 1 per cent level were observed in the blue region and attributed to Si II, Mg II and Fe II lines (Wang et al. 2006). Furthermore, the Si II $\lambda$6355 line was unusually strong in polarization, with a level of $\sim 1.7-1.8$ per cent at peak (see also Fig. 13). Taken together, these properties make SN 2004dt the most polarized SN Ia ever observed.

Fig. 12 shows pre- and post-maximum polarization spectra of SN 2004dt together with those extracted for the two explosion models studied in this paper. The agreement in the flux spectra of the models with SN 2004dt is of comparable quality to that with SN 2001el and SN 2012fr. However, we clearly see that none of the orientations investigated for the D-DET and N100-DDT model can reproduce the degrees of polarization observed in SN 2004dt. In contrast, a better match to SN 2004dt was found by Bulla et al. (2016) for the least polarized line of sights of the violent merger of Pakmor et al. (2012). Although both explosion models studied in this paper reproduce the flux spectra comparably well to the violent merger model, spectropolarimetry does provide a very clear distinction. Specifically, for both models, the synthetic spectropolarimetry hardly ever exceeds a level of 0.5 per cent, which is clearly insufficient to account for the exceptional polarization levels of SN 2004dt.

### 5.2 Polarization of the Si II $\lambda$6355 feature

Si II $\lambda$6355, one of the hallmark features in the spectra of SNe Ia, is generally found to be polarized. Around maximum light the degree of polarization is typically below 1 per cent, although larger values are also found (see Wang et al. 2007). In this section, we compare the distribution of values observed in normal SNe Ia with those predicted in this study for the D-DET and N100-DDT model. Observed values include 16 normal SNe Ia from Wang et al. (2007), SN 2006X from Patat et al. (2009), SN 2012fr from Maund et al. (2013) and SN 2014J from Patat et al. (2014) and Porter et al. (2016). To facilitate the comparison with data, we follow the convention of Wang et al. (2007) and present synthetic polarization values estimated via Gaussian fitting of the Si II $\lambda$6355 profile at 5 d before $B-$band maximum light. To explore the full range of polarization covered by each model, here we also include predictions from our low signal-to-noise calculations with spectra extracted for an additional 17 (D-DET) and 21 (N100-DDT) orientations (see Section 3.1).

Fig. 13 shows the solid-angle-weighted distribution of Si II $\lambda$6355 polarization values extracted for our models compared to those detected in normal SN Ia events. This comparison clearly demonstrates that our models produce polarization signals in a range ($\lesssim$ 1 per cent) comparable to the values observed. Although the range of polarization predicted by the two models is relatively similar, the D-DET model typically produces lower levels of polarization than the N100-DDT model (in line with the findings of Section 4) and it provides a good match with observed SNe at the low-polarization end of the distribution. Nonethe-

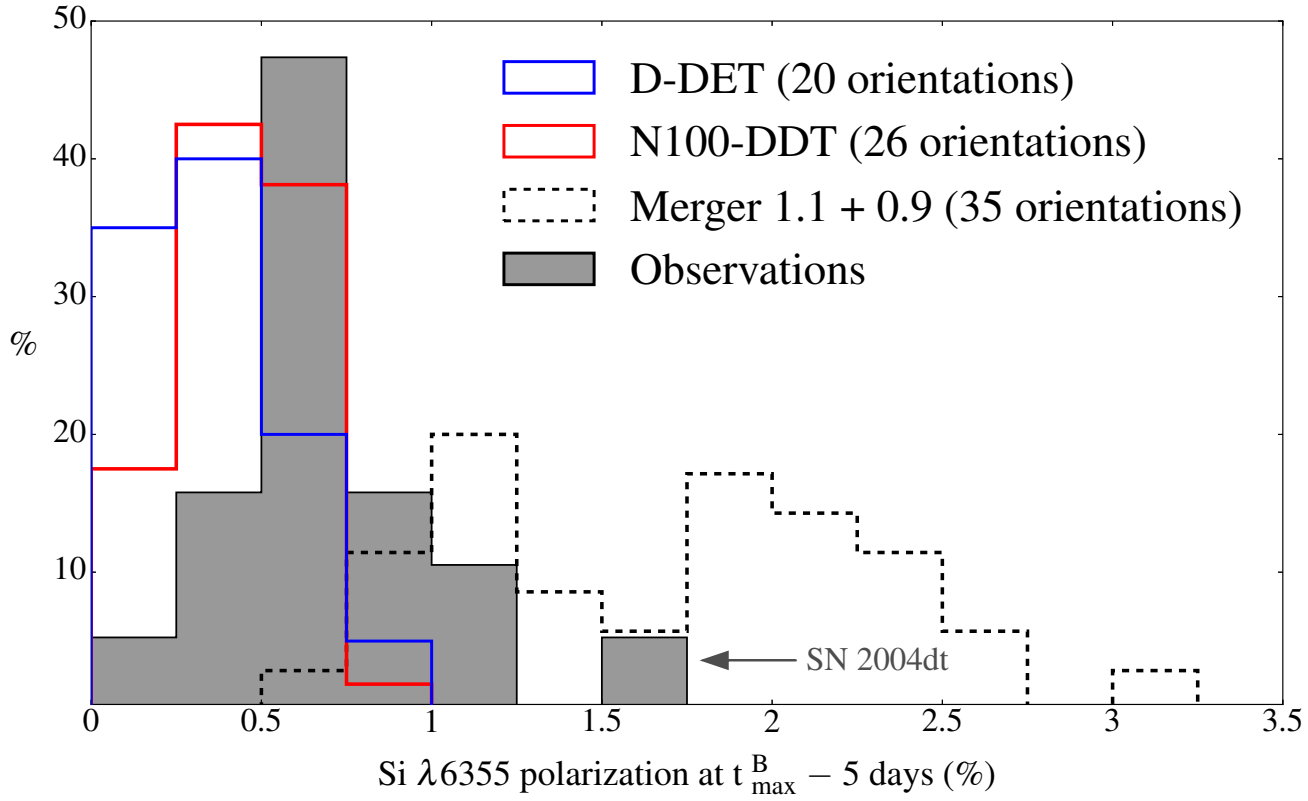


**Figure 13.** Solid-angle-weighted distribution of Si II $\lambda$6355 polarization at 5 d before $B-$band maximum for the D-DET (blue distribution) and N100-DDT (red distribution) models, together with the distribution of values observed for normal SNe Ia (grey distribution, Wang et al. 2007; Patat et al. 2009; Maund et al. 2013; Patat et al. 2014; Porter et al. 2016). The distribution of each explosion model includes orientations from both high and low signal-to-noise calculations (see Section 3.1). For comparison, the dashed purple distribution reports values extracted along 35 different viewing angles for the violent merger model of Pakmor et al. (2012, see Bulla et al. 2016).

less, neither the D-DET nor the N100-DDT model can account for the relatively high Si II $\lambda$6355 polarization levels ($\gtrsim$ 1 per cent) observed in a handful of SNe Ia (Wang et al. 2007; Patat et al. 2009). We note, however, that polarization signals for objects at the upper end of the distribution are associated with high-velocity components of the Si II $\lambda$6355 profile. As none of our explosion models is able to produce high-velocity features in the Si II $\lambda$6355 line, it is not surprising that the match in polarization with these relatively highly-polarized objects is also poor.

For comparison, in Fig. 13 we also include polarization values extracted for the violent merger model of Pakmor et al. (2012) along 35 different orientations (Bulla et al. 2016). As discussed by Bulla et al. (2016), compared to observations, the silicon line is typically too highly polarized in this model, with levels above 1.75 per cent for about half of the orientations. However, predictions for the remaining orientations match the polarization observed for "highly"-polarized events ($\gtrsim$ 1 per cent) like SN 2004dt (see also fig. 11 of Bulla et al. 2016).

### 5.3 Polarization of the O I / Si II / Mg II feature

Unlike the cases of Si II and Ca II, no unambiguous polarization signature has ever been observed for the O I feature in SNe Ia (Wang & Wheeler 2008). In particular, even when investigating relatively polarized objects as SN 2004dt and SN 2006X, Wang et al. (2006) and Patat et al. (2009) were only able to place upper limits of $\sim$ 0.3 per cent on the O I $\lambda$7774 degree of polarization. Based on the spectropolarimetric data of SN 2004dt, Wang et al. (2006) have interpreted the fact that silicon, calcium and oxygen features are seen at similar velocities, but with different polarimetric properties, as evidence that aspherically-distributed IMEs should spatially coexist with the more spherically-distributed oxygen layer. This interpretation was supported by predictions from delayed-detonation models deformed into ellipsoidal geometries (Howell et al. 2001; Höflich et al. 2006). As shown in Fig. 1, the distribution of oxygen, calcium and silicon in the ejecta of our models is consistent with this interpretation. Indeed, as expected, the more spherical distribution of oxygen, compared to those of silicon and calcium, results in weaker polarization levels across the O I $\lambda$7774 region than across the Si II and Ca II lines.

Despite being weak, however, polarization signatures in the O I $\lambda$7774 wavelength region are clearly discernible in both our models and may be detectable with slightly more sensitive spectropolarimetric observations. In particular, in Section 4.2 we have seen that the polarization peaks around this region can be associated with either O I $\lambda$7774, Si II $\lambda$7849, Mg II $\lambda$7887 or a mixture of these three lines. In Fig. 14 we show a zoom into the O I $\lambda$7774 region for

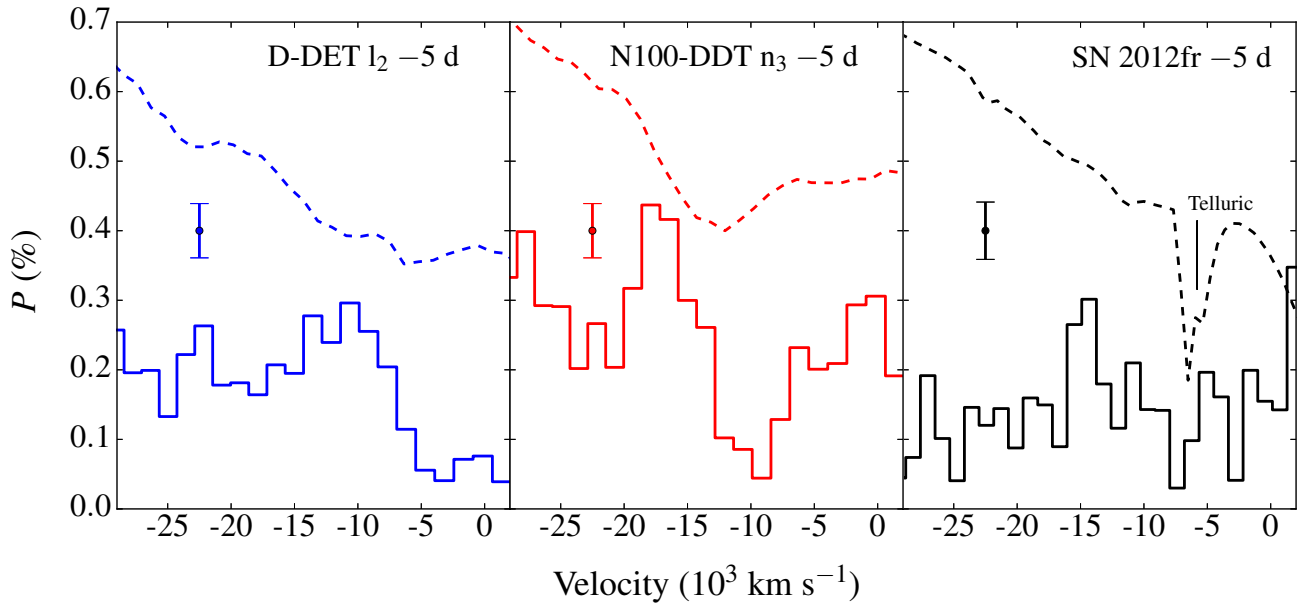


**Figure 14.** Polarization spectra (solid lines) around the O I $\lambda$7774 feature at 5 d before maximum. Spectra extracted for the D-DET $\boldsymbol{l_2}$ (left-hand panel) and the N100-DDT $\boldsymbol{n_3}$ (middle panel) orientations are reported together with those observed for SN 2012fr (right-hand panel). Flux spectra are arbitrarily scaled for presentation and reported with dashed lines in each panel. Error bars mark the uncertainties on the synthetic (left-hand and middle panels) and observed (right-hand panel) polarization spectra.

the observed spectra of SN 2012fr and the synthetic spectra predicted by our models. Spectra are reported at 5 d before maximum and are the same as in the left-hand panels of Fig. 10. Polarization peaks at the 0.3 and 0.4 per cent level are predicted across this spectral region by both explosion models. A similar analysis to that presented in Section 4.2 suggests that the polarization signal across this feature is dominated by O I $\lambda$7774 for both these orientation/model/epoch combinations, and the predicted velocities for this feature are $\sim -10\,000$ km s$^{-1}$ for the D-DET and $\sim -17\,000$ km s$^{-1}$ for the N100-DDT model. Although Maund et al. (2013) did not discuss any possible signal associated with O I $\lambda$7774, we notice a marginal increase in the polarization levels up to $\sim 0.2-0.3$ per cent between $-10\,000$ and $-15\,000$ km s$^{-1}$ that, owing to the resemblance with the predicted profiles, might be associated with O I $\lambda$7774.

Overall, we conclude that the spectral region around the O I / Si II / Mg II feature is an interesting target for future spectropolarimetric observations since the models predict that weak signatures may be present here. In addition, predictions from the D-DET model suggest that these signatures may be observed rotated of 90° with respect to Si II $\lambda$6355, Ca II IR and other lines in the spectrum. However, we caution that interpretation will be complicated by the competing roles of the O I, Si II and Mg II spectral features in this range for which the relative contributions is likely to vary as a function of epoch and observer orientation, as highlighted by the discussion in Section 4.2.

### 5.4 Polarization of the Ca II IR triplet feature

As shown in Section 5.1, our two explosion models fail to reproduce the polarization signatures observed in SNe Ia across the Ca II IR triplet feature. The disagreement is particularly evident across the high-velocity ($\sim 15\,000-20\,000$ km s$^{-1}$) components of this line that are frequently detected in both intensity (e.g. Gerardy et al. 2004; Mazzali et al. 2005a; Childress et al. 2014; Maguire et al. 2014; Silverman et al. 2015; Zhao et al. 2015) and polarization (e.g. Wang et al. 2003; Maund et al. 2013) spectra of SNe Ia.

In the N100-DDT model, typical values for the velocities ($\sim 12\,000-15\,000$ km s$^{-1}$) and the polarization signals ($\sim 0.3$ per cent) extracted across the Ca II IR triplet line are too low to match the observations, as highlighted by the spectral comparison with SN 2001el (Fig. 11) and SN 2012fr (Fig. 10). This comes as no surprise, since the calcium distribution in the ejecta of this model extends up to $\sim 15\,000$ km s$^{-1}$ and is not strongly asymmetric (see Fig. 1).

The D-DET model appears more promising in matching the calcium high-velocity components since the distribution of calcium in this model can reach up to $\sim 30\,000$ km s$^{-1}$ for orientations close to the north pole. Indeed, we find a reasonable match between velocities predicted for the D-DET model along the equatorial direction ($\boldsymbol{l_2}$) and those observed in both SN 2001el (Fig. 11) and SN 2012fr (Fig. 10). This orientation, however, is associated with polarization signals across the calcium line that are inconsistent with data. Because of the strong asymmetries in the outer shell of this model (see Fig. 1), selecting orientations out of the equatorial plane typically leads to poorer matches with observations: calcium lines for viewing angles in the southern hemisphere are typically too weakly polarized and too slow, while those in the northern hemisphere too strongly polarized and too fast (see polarization spectra around maximum light in Fig. 2).

Although high-velocity features in the Ca II IR triplet are frequently observed in SN Ia spectra, their origin remains unclear and may be associated with either a density increase (Gerardy et al. 2004; Mazzali et al. 2005b; Tanaka et al. 2006), a composition enhancement (Mazzali et al. 2005b) or a ionization effect (Blondin et al. 2013) in the outer ejecta. In the single-degenerate scenario, a density increase might be associated with circumstellar material (Gerardy et al. 2004; Mazzali et al. 2005b; Tanaka et al. 2006). If that is the case, the lack of high-velocity features in the N100-DDT model would not be surprising as circumstellar material is not captured by the Seitenzahl et al. (2013) explosion models. Alternatively, an abundance enhancement in the outer regions of the ejecta (Mazzali et al. 2005b) would seem qualitatively consistent with the calcium distribution predicted in the He-shell by our D-DET model. As noted above, however, the D-DET model struggles to simultaneously reproduce spectroscopic and polarimetric properties of this high-velocity material. In the future development of double-detonation models, it will be then particularly important to consider whether better agreement in the high-velocity Ca II features can be achieved by models in which properties of the ash of the He-shell detonation (both composition and geometry) differ from the predictions of the Fink et al. (2010) simulations. In particular, we note that it has already been suggested that changes in the He-shell properties are likely required if such models are to provide a good match to observed optical light curves and colours (see e.g. Kromer et al. 2010). It remains to be seen whether multi-dimensional explosion models with altered He shell properties can produce morphologies more consistent with the observed spectropolarimetry of high-velocity features.

## 6 DISCUSSION AND CONCLUSIONS

We have presented polarization calculations for one double-detonation model from Fink et al. (2010, here referred to as D-DET) and one delayed-detonation model from Seitenzahl et al. (2013, here N100-DDT). Using the techniques of Bulla et al. (2015), we calculated polarization spectra around maximum light and focused on three orientations for the 2D D-DET model and five for the 3D N100-DDT model. In order to map out the range of polarization covered by the models, we also performed extra-calculations that provide lower signal-to-noise spectra for an additional 17 (D-DET) and 21 (N100-DDT) viewing angles.

For both models, the overall polarization levels are low at all the epochs considered in this study (between 10 and 30 d after explosion): they are consistently below 1 per cent, with the largest values generally observed for the N100-DDT model. While the 2D D-DET model is axi-symmetric by construction, polarization spectra for the 3D N100-DDT model verify that polarimetry could be used to identify deviations from a single-axis geometry. A common behaviour between the two explosion models is the relative rise in polarization level from blue to red wavelengths. Our calculations confirm that this effect, which is regularly observed in both normal (e.g. Wang et al. 1997) and subluminous (e.g. Howell et al. 2001) SNe Ia, can be ascribed to the decreasing line blanketing when moving to longer wavelengths, and is fairly well captured in the explosion models: in our simulations around maximum light, the fraction of escaping packets having a depolarizing line interaction as last event drops from about 0.8 at 4000 Å to only 0.3 at 7000 Å.

Polarization spectra predicted by our models match particularly well those observed for the majority of normal SNe Ia, as clearly highlighted by the comparison with the two well-studied supernovae SN 2001el and SN 2012fr. Polarization levels in the pseudo-continuum range (between 6500 and 7500 Å) are found to decrease from $\sim 0.1-0.3$ per cent at maximum light to lower values at later times, in strikingly good agreement with observations. Higher degrees of polarization are predicted at wavelengths corresponding to the troughs of absorption lines. In particular, the set of polarization signals extracted across the Si II $\lambda$6355 feature ($\lesssim 1$ per cent) provides a remarkable match with the distribution of values observed in normal SNe Ia (Wang et al. 2007; Patat et al. 2009; Maund et al. 2013), while the low degrees of polarization found in the O I $\lambda$7774 region are consistent with the non-detection of this feature in currently available data. Taken together, these findings lead us to conclude that the geometries of both the explosion models considered here are likely to be broadly consistent with those of normal SNe Ia.

However, none of our models is able to reproduce the high-velocity ($\sim 15\,000-20\,000$ km s$^{-1}$) components of the Ca II IR triplet and Si II $\lambda$6355 lines that are frequently observed in both intensity (e.g. Gerardy et al. 2004; Mazzali et al. 2005a; Childress et al. 2014; Maguire et al. 2014; Silverman et al. 2015; Zhao et al. 2015) and polarization (e.g. Wang et al. 2003; Leonard et al. 2005; Wang et al. 2006; Maund et al. 2013) spectra of SNe Ia. Although the D-DET scenario is more promising in this sense – as the calcium in the outer shell of this model leads to velocities in the right range for some orientations – none of our models is able to simultaneously produce the spectroscopic and polarimetric signatures characteristic of this high-velocity material. The failure to predict silicon and calcium in the right location and with the right geometry clearly indicates that more work is needed to understand whether the two scenarios investigated in this study can account for the high-velocity features observed in the Si II $\lambda$6355 and Ca II IR triplet lines.

The two models presented in this paper are hard to distinguish based on their polarization signatures. In both, polarizing electron scattering contributions originate in rather spherical regions of the ejecta (between $\sim$ 5000 and 15 000 km s$^{-1}$), thus leading to polarization levels that are typically low and similar for the two models at most wavelengths. It is important to note, however, that we have only calculated polarization signatures for two specific models and the results presented here are not necessarily representative of the whole Fink et al. (2010) double-detonation and Seitenzahl et al. (2013) DDT studies. While the different double-detonation models of Fink et al. (2010) are all characterized by relatively similar geometries – and are thus expected to produce comparable polarization signals – the DDT models of Seitenzahl et al. (2013) yield ejecta whose morphologies are strongly dependent on the ignition configuration (see also Section 2.2). In particular, compared to the N100 model used in this paper, models in which the explosion is initiated with a smaller number of kernels (1 to 40) are typically more asymmetric and thus likely to be more polarized. In the future, it will be crucial to map out

the polarization range spanned by the full set of models of Fink et al. (2010) and Seitenzahl et al. (2013) to understand whether the two scenarios can be effectively distinguished via variations between the polarization signatures across the model sequences.

This study is part of a long-term project aimed to test multi-dimensional hydrodynamic explosion models via their polarization signatures. In a previous paper (Bulla et al. 2016), we have demonstrated that the violent merger of a 1.1 and a 0.9 $M_\odot$ WD (Pakmor et al. 2012) is unlikely to explain polarization features observed for the bulk of normal SNe Ia. In contrast, this work shows that the realizations of the double-detonation and DDT scenarios studied here produce polarization levels in much better agreement with spectropolarimetric data of normal SNe Ia. To investigate whether the polarization properties of the discussed model classes are representative for the observed SN Ia population, in the future we aim to map out the parameter space of all the three explosion scenarios.

## ACKNOWLEDGEMENTS

We thank the anonymous reviewer for his/her valuable comments. We are grateful to Douglas Leonard and Justyn Maund for providing polarization data of SN 2004dt and SN 2012fr reported in this work. MB thanks Ferdinando Patat for many useful discussions about modelling and observing polarized light from supernovae.

This work used the DiRAC Complexity system, operated by the University of Leicester IT Services, which forms part of the STFC DiRAC HPC Facility (www.dirac.ac.uk). This equipment is funded by BIS National E-Infrastructure capital grant ST/K000373/1 and STFC DiRAC Operations grant ST/K0003259/1. DiRAC is part of the National E-Infrastructure.

This research was supported by the Partner Time Allocation (Australian National University), the National Computational Merit Allocation and the Flagship Allocation Schemes of the NCI National Facility at the Australian National University. Parts of this research were conducted by the Australian Research Council Centre of Excellence for All-sky Astrophysics (CAASTRO), through project number CE110001020.

The authors gratefully acknowledge the Gauss Centre for Supercomputing (GCS) for providing computing time through the John von Neumann Institute for Computing (NIC) on the GCS share of the supercomputer JUQUEEN (Stephan & Docter 2015) at Jülich Supercomputing Centre (JSC). GCS is the alliance of the three national supercomputing centres HLRS (Universität Stuttgart), JSC (Forschungszentrum Jülich), and LRZ (Bayerische Akademie der Wissenschaften), funded by the German Federal Ministry of Education and Research (BMBF) and the German State Ministries for Research of Baden-Württemberg (MWK), Bayern (StMWFK) and Nordrhein-Westfalen (MIWF).

SAS acknowledges support from STFC grant ST/L0000709/1. IRS was supported by the Australian Research Council Laureate Grant FL0992131. The work of FKR and RP is supported by the Klaus Tschira Foundation. RP acknowledges support by the European Research Council under ERC-StG grant EXAGAL-308037, WH and ST by the DFG through the Cluster of Excellence 'Origin and Structure of the Universe' and the Transregio Project 33 'The Dark Universe'.

## REFERENCES

Bildsten L., Shen K. J., Weinberg N. N., Nelemans G., 2007, ApJL, 662, L95
Blondin S., Dessart L., Hillier D. J., 2015, MNRAS, 448, 2766
Blondin S., Dessart L., Hillier D. J., Khokhlov A. M., 2013, MNRAS, 429, 2127
Bulla M., Sim S. A., Kromer M., 2015, MNRAS, 450, 967
Bulla M., Sim S. A., Pakmor R., Kromer M., Taubenberger S., Röpke F. K., Hillebrandt W., Seitenzahl I. R., 2016, MNRAS, 455, 1060
Childress M. J., Filippenko A. V., Ganeshalingam M., Schmidt B. P., 2014, MNRAS, 437, 338
Childress M. J., Hillier D. J., Seitenzahl I., Sullivan M., Maguire K., Taubenberger S., Scalzo R., Ruiter A., Blagorodnova N., Camacho Y., et al., 2015, MNRAS, 454, 3816
Ciaraldi-Schoolmann F., Seitenzahl I. R., Röpke F. K., 2013, A&A, 559, A117
Fink M., Hillebrandt W., Röpke F., 2007, A&A, 476, 1133
Fink M., Röpke F. K., Hillebrandt W., Seitenzahl I. R., Sim S. A., Kromer M., 2010, A&A, 514, A53
Fransson C., Jerkstrand A., 2015, ApJL, 814, L2
Gall E., Taubenberger S., Kromer M., Sim S., Benetti S., Blanc G., Elias-Rosa N., Hillebrandt W., 2012, MNRAS, 427, 994
Gerardy C. L., Höflich P., Fesen R. A., Marion G. H., Nomoto K., Quimby R., Schaefer B. E., Wang L., Wheeler J. C., 2004, ApJ, 607, 391
Hachisu I., Kato M., Nomoto K., 2008, ApJL, 683, L127
Hamilton D. R., 1947, ApJ, 106, 457
Hillebrandt W., Kromer M., Röpke F., Ruiter A., 2013, Frontiers of Physics, 8, 116
Höflich P., Gerardy C. L., Marion H., Quimby R., 2006, New Astronomy Reviews, 50, 470
Höflich P., Khokhlov A., 1996, ApJ, 457, 500
Höflich P., Khokhlov A. M., Wheeler J. C., 1995, ApJ, 444, 831
Howell D. A., Höflich P., Wang L., Wheeler J. C., 2001, ApJ, 556, 302
Jeffery D. J., 1989, ApJS, 71, 951
Jeffery D. J., 1991, ApJ, 375, 264
Kasen D., Nugent P., Thomas R. C., Wang L., 2004, ApJ, 610, 876
Kasen D., Nugent P., Wang L., Howell D., Wheeler J. C., Höflich P., Baade D., Baron E., Hauschildt P., 2003, ApJ, 593, 788
Kasen D., Röpke F. K., Woosley S. E., 2009, Nature, 460, 869
Khokhlov A. M., 1991, A&A, 245, 114
Kosenko D., Hillebrandt W., Kromer M., Blinnikov S., Pakmor R., Kaastra J., 2015, MNRAS, 449, 1441
Kromer M., Sim S. A., 2009, MNRAS, 398, 1809
Kromer M., Sim S. A., Fink M., Röpke F. K., Seitenzahl I. R., Hillebrandt W., 2010, ApJ, 719, 1067

Leonard D. C., Filippenko A. V., Ardila D. R., Brotherton M. S., 2001, ApJ, 553, 861
Leonard D. C., Li W., Filippenko A. V., Foley R. J., Chornock R., 2005, ApJ, 632, 450
Livne E., 1990, ApJ, 354, L53
Livne E., Glasner A. S., 1990, ApJ, 361, 244
Maguire K., Sullivan M., Pan Y.-C., Gal-Yam A., Hook I. M., Howell D. A., Nugent P. E., Mazzali P., Chotard N., Clubb K. I., et al., 2014, MNRAS, 444, 3258
Maoz D., Mannucci F., Nelemans G., 2014, ARA&A, 52
Maund J. R., Spyromilio J., Höflich P. A., Wheeler J. C., Baade D., Clocchiatti A., Patat F., Reilly E., Wang L., Zelaya P., 2013, MNRASL, 433, L20
Mazzali P. A., Benetti S., Altavilla G., Blanc G., Cappellaro E., Elias-Rosa N., Garavini G., Goobar A., Harutyunyan A., Kotak R., et al., 2005, ApJL, 623, L37
Mazzali P. A., Benetti S., Stehle M., Branch D., Deng J., Maeda K., Nomoto K., Hamuy M., 2005, MNRAS, 357, 200
Mennekens N., Vanbeveren D., De Greve J., De Donder E., 2010, A&A, 515, A89
Moll R., Woosley S., 2013, ApJ, 774, 137
Niemeyer J. C., Woosley S. E., 1997, ApJ, 475, 740
Nomoto K., 1980, Space Science Reviews, 27, 563
Pakmor R., Kromer M., Taubenberger S., Sim S. A., Röpke F. K., Hillebrandt W., 2012, ApJL, 747, L10
Patat F., Baade D., Höflich P., Maund J. R., Wang L., Wheeler J. C., 2009, A&A, 508, 229
Patat F., Höflich P., Baade D., Maund J., Wang L., Wheeler J., 2012, A&A, 545, A7
Patat F., Romaniello M., 2006, PASP, 118, 146
Patat F., Taubenberger S., Baade D., Hoeflich P., Maund J., Reilly E., Spyromilio J., Wang L., Wheeler J. C., Zelaya P., 2014, The Astronomer's Telegram, 5830
Perlmutter S., Aldering G., Goldhaber G., Knop R., Nugent P., Castro P., Deustua S., Fabbro S., Goobar A., Groom D., et al., 1999, ApJ, 517, 565
Plewa T., Calder A. C., Lamb D. Q., 2004, ApJL, 612, L37
Porter A. L., Leising M. D., Williams G. G., Milne P., Smith P., Smith N., Bilinski C., Hoffman J. L., Huk L., Leonard D. C., 2016, ApJ, preprint (arXiv:1605.03994)
Riess A. G., Filippenko A. V., Challis P., Clocchiatti A., Diercks A., Garnavich P. M., Gilliland R. L., Hogan C. J., Jha S., Kirshner R. P., et al., 1998, ApJ, 116, 1009
Röpke F., Niemeyer J., 2007, A&A, 464, 683
Röpke F., Woosley S., Hillebrandt W., 2007, ApJ, 660, 1344
Röpke F. K., Kromer M., Seitenzahl I. R., Pakmor R., Sim S. A., Taubenberger S., Ciaraldi-Schoolmann F., Hillebrandt W., Aldering G., Antilogus P., et al., 2012, ApJL, 750, L19
Ruiter A., Belczynski K., Sim S. A., Hillebrandt W., Fryer C., Fink M., Kromer M., 2011, MNRAS, 417, 408
Scalzo R., Aldering G., Antilogus P., Aragon C., Bailey S., Baltay C., Bongard S., Buton C., Cellier-Holzem F., Childress M., et al., 2014, MNRAS, 440, 1498
Scalzo R., Ruiter A., Sim S., 2014, MNRAS, 445, 2535
Seitenzahl I. R., Ciaraldi-Schoolmann F., Röpke F. K., Fink M., Hillebrandt W., Kromer M., Pakmor R., Ruiter A. J., Sim S. A., Taubenberger S., 2013, MNRAS, 429, 1156
Shen K. J., Bildsten L., 2009, ApJ, 699, 1365
Silverman J. M., Vinkó J., Marion G., Wheeler J. C., Barna B., Szalai T., Mulligan B. W., Filippenko A. V., 2015, MNRAS, 451, 1973
Sim S. A., 2007, MNRAS, 375, 154
Sim S. A., Seitenzahl I. R., Kromer M., Ciaraldi-Schoolmann F., Röpke F. K., Fink M., Hillebrandt W., Pakmor R., Ruiter A. J., Taubenberger S., 2013, MNRAS, 436, 333
Sneden C., Cowan J. J., Kobayashi C., Pignatari M., Lawler J. E., Den Hartog E. A., Wood M. P., 2016, ApJ, 817, 53
Stephan M., Docter J., 2015, Journal of large-scale research facilities JLSRF, 1
Stritzinger M., Mazzali P., Sollerman J., Benetti S., 2006, A&A, 460, 793
Summa A., Ulyanov A., Kromer M., Boyer S., Röpke F. K., Sim S. A., Seitenzahl I. R., Fink M., Mannheim K., Pakmor R., et al., 2013, A&A, 554, A67
Taam R. E., 1980, ApJ, 237, 142
Tanaka M., Mazzali P. A., Maeda K., Nomoto K., 2006, ApJ, 645, 470
Wang L., Baade D., Höflich P., Khokhlov A., Wheeler J. C., Kasen D., Nugent P. E., Perlmutter S., Fransson C., Lundqvist P., 2003, ApJ, 591, 1110
Wang L., Baade D., Höflich P., Wheeler J. C., Kawabata K., Khokhlov A., Nomoto K., Patat F., 2006, ApJ, 653, 490
Wang L., Baade D., Patat F., 2007, Science, 315, 212
Wang L., Wheeler J. C., 2008, ARA&A, 46, 433
Wang L., Wheeler J. C., Höflich P., 1997, ApJL, 476, L27
Zhao X., Wang X., Maeda K., Sai H., Zhang T., Zhang J., Huang F., Rui L., Zhou Q., Mo J., 2015, ApJS, 220, 20